

FABRICATION AND CHARACTERIZATION OF InP BASED QUANTUM
WELL INFRARED PHOTODETECTORS

A THESIS SUBMITTED TO
THE GRADUATE SCHOOL OF NATURAL AND APPLIED SCIENCES
OF
MIDDLE EAST TECHNICAL UNIVERSITY

BY

GAMZE TORUNOĞLU

IN PARTIAL FULFILLMENT OF THE REQUIREMENTS
FOR
THE DEGREE OF MASTER OF SCIENCE
IN
MICRO AND NANOTECHNOLOGY PROGRAM

JUNE 2012

Approval of the thesis:

**FABRICATION AND CHARACTERIZATION OF InP BASED QUANTUM
WELL INFRARED PHOTODETECTORS**

submitted by **GAMZE TORUNOĞLU** in partial fulfillment of the requirements
for the degree of **Master of Science in Micro and Nanotechnology Program,**
Middle East Technical University by,

Prof. Dr. Canan Özgen
Dean, Graduate School of **Natural and Applied Sciences**

Prof. Dr. Mürvet Volkan
Head of Department, **Micro and Nanotechnology Prog.**

Prof. Dr. Cengiz Beşikçi
Supervisor, **Electrical and Electronics Eng. Dept., METU**

Examining Committee Members:

Prof. Dr. Mehmet Parlak
Physics Dept., METU

Prof. Dr. Cengiz Beşikçi
Electrical and Electronics Engineering Dept., METU

Assoc. Prof. Dr. Özgür Aktaş
Electrical and Electronics Engineering Dept., METU

Prof. Dr. Nevzat Gençer
Electrical and Electronics Engineering Dept., METU

Prof. Dr. Raşit Turan
Physics Dept., METU

Date: 29.06.2012

I hereby declare that all information in this document has been obtained and presented in accordance with academic rules and ethical conduct. I also declare that, as required by these rules and conduct, I have fully cited and referenced all material and results that are not original to this work.

Name, Last name: GAMZE TORUNOĞLU

Signature :

ABSTRACT

FABRICATION AND CHARACTERIZATION OF InP BASED QUANTUM WELL INFRARED PHOTODETECTORS

TORUNOĞLU, Gamze

M.Sc., Department of Micro and Nanotechnology

Supervisor: Prof. Dr. Cengiz BEŞİKCI

Co-supervisor: Prof. Dr. Mehmet PARLAK

JUNE 2012, 70 pages

Quantum Well Infrared Photodetectors (QWIPs) have the advantages of excellent uniformity and mature material properties. Thanks to these properties, large format and low cost QWIP focal plane arrays (FPAs) can be fabricated. The standard material system used for QWIP FPAs is AlGaAs/GaAs in the long wavelength infrared (LWIR) band. AlGaAs/GaAs material system has some disadvantages such as low quantum and conversion efficiencies under high frame rate and/or low background conditions. These limitations of the standard material system give rise to research on alternative material systems for QWIPs. InP/InGaAs material system is an alternative to AlGaAs/GaAs for LWIR QWIPs. This thesis focuses on the development of InP/InGaAs QWIP FPAs. A large format (640x512) LWIR QWIP FPA constructed with strained InP/InGaAs system is demonstrated with high quantum and conversion efficiencies. The FPA fabricated with the 40-well epilayer

structure yielded a peak quantum efficiency as high as 20% with a broad spectral response ($\Delta\lambda/\lambda_p=15\%$). The responsivity peak and the cut-off wavelengths of the FPA are 8.5 and $\sim 9 \mu\text{m}$, respectively. The peak responsivity of the FPA pixels is larger than 1 A/W with a conversion efficiency as high as $\sim 17\%$ in the bias region where the detectivity is reasonably high. The FPA provides a background limited performance (BLIP) temperature higher than 65 K ($f/1.5$) and satisfies the requirements of most low integration time/low background applications. Noise equivalent temperature difference (NETD) of the FPA is as low as 25 mK with integration times as short as 2 ms ($f/1.5$, 68 K).

Keywords: QWIP, LWIR, FPA, InP

ÖZ

InP TEMELLİ KUANTUM KUYULU KIZILÖTESİ FOTODEDEKTÖRLERİN ÜRETİMİ VE KARAKTERİZASYONU

TORUNOĞLU, Gamze

Yüksek Lisans, Mikro ve Nanoteknoloji Bölümü

Tez Danışmanı: Prof. Dr. Cengiz BEŞİKÇİ

Ortak Tez Danışmanı: Prof. Dr. Mehmet PARLAK

Haziran 2012, 70 sayfa

Kuantum Kuyulu Kızılötesi Fotodedektörler (KKKF) yüksek homojenlik ve olgun malzeme özellikleri avantajlarına sahiptir. Bu özelliklerinden dolayı KKKF odak düzlem dizinleri (ODD) geniş formatlı ve düşük maliyetli olarak üretilebilmektedir. Uzun dalgaboyu kızılötesi (UDK) bandında kullanılan standart malzeme sistemi AlGaAs/GaAs sistemidir. AlGaAs/GaAs malzeme sistemi yüksek resim hızlarında ve/veya alçak arkaplan durumlarında düşük kuantum ve çevirim verimliliği gibi dezavantajlara sahiptir. Standart malzeme sisteminin bu kısıtlamaları alternatif malzeme sistemlerinin araştırılmasına neden olmaktadır. InP/InGaAs malzeme sistemi UDK KKKF'ler için AlGaAs/GaAs malzeme sistemine bir alternatiftir. Bu tez, InP/InGaAs KKKF ODD'lerin geliştirilmesine odaklanmıştır. Yüksek kuantum ve çevirim verimliliğine sahip olup gerilimli InP/InGaAs malzeme sistemi ile üretilmiş, geniş formatlı (640x512) bir UDK KKKF ODD gösterilmiştir. 40

kuantum kuyulu epikatman yapısıyla üretilen ODD, geniş bir tepkisellik spektrumuyla ($\Delta\lambda/\lambda_p=15\%$) %20 mertebesinde tepe kuantum verimliliği vermiştir. ODD'nin tepkisellik tepe ve kesim dalgaboyları sırasıyla 8.5 ve $\sim 9 \mu\text{m}$ 'dir. Dedektivitenin yeteri kadar yüksek olduğu gerilim aralığında % 17 civarında çevirim verimliliği ile ODD piksellerinin tepe tepkiselliği 1 A/W'dan daha yüksektir. ODD, 65 K'den daha yüksek sıcaklıklarda ($f/1.5$) arka plan sınırlı performans (APSP) sağlamakta ve düşük entegrasyon zamanı/düşük arka plan uygulamalarının gereksinimlerini karşılamaktadır. ODD'nin gürültü eşdeğer sıcaklık farkı (GESF) 2 ms gibi kısa entegrasyon zamanlarıyla 25 mK kadar düşük seviyededir ($f/1.5$, 68K).

Anahtar Kelimeler: KKKF, UDK, ODD, InP

To my lovely son Metin

ACKNOWLEDGEMENTS

First, I would like to thank my advisor Prof. Dr. Cengiz Beşikci for his guidance and supervision and providing me the possibility to work in such a sophisticated facility.

I would like to thank Prof. Dr. Mehmet Parlak, Prof. Dr. Raşit Turan, Prof. Dr. Nevzat Gençer and Assoc.Prof. Özgür Aktaş for being on my thesis committee.

I would like to express my gratitude to Yetkin Arslan for his invaluable support throughout this study and sharing with me his knowledge and experience with FPA fabrication processes and characterization as well as his friendship.

I would like to thank to Dr. Tahir Çolakoğlu, Birce Boyacı, İlgi Koçer, Volkan Hünerli and Sırma Hörgüç for their friendships and help in all the laboratory work.

I would like to thank Özgür Şen for the extraordinary energy and effort to keep the laboratory running and for his friendship.

I would like to thank all of the past and present members of our research group for their friendship.

Last but not the least, I want to express my deep love and gratitude to my husband Emin and my family for their never ending support.

TABLE OF CONTENTS

ABSTRACT	iv
ÖZ.....	vi
DEDICATION	viii
ACKNOWLEDGMENTS.....	ix
TABLE OF CONTENTS	x
LIST OF TABLES	xii
LIST OF FIGURES.....	xiii
CHAPTERS	
1. INTRODUCTION.....	1
1.1 Infrared Radiation.....	2
1.1.1 Blackbody Radiation.....	3
1.1.2 Atmospheric Transmission.....	4
1.1.3 Choice of Infrared Band.....	6
1.2 Infrared Detectors	7
1.2.1 Thermal Detectors	7
1.2.2 Photon Detectors	8
1.3 Figures of Merits for Infrared Detectors.....	12
1.3.1 Responsivity	13
1.3.2 Noise.....	13
1.3.3 Detectivity	15
1.3.4 Noise Equivalent Temperature Difference (NETD)	16

1.4	Objective of This Thesis Work.....	17
2.	QUANTUM WELL INFRARED PHOTODETECTORS.....	18
2.1	Theory of Operation	18
2.1.1	Optical Coupling	23
2.1.2	Dark Current.....	25
2.1.3	Responsivity and Photoconductive Gain	27
2.1.4	Noise.....	29
2.1.5	Detectivity	29
2.2	Material Systems for QWIPs.....	30
2.3	Fabrication of QWIP Focal Plane Arrays.....	31
2.4	QWIP versus HgCdTe Photodetectors	35
2.5	State of the Art in QWIPs.....	36
3.	InP BASED LWIR QWIP TECHNOLOGY	42
3.1	Advantages of InP based QWIPs.....	42
3.2	QWIP Design on InP Substrate	48
3.3	InP/InGaAs LWIR QWIPs	50
3.3.1	QWIP Epilayer Structure	50
3.3.2	InP/InGaAs QWIP FPA on InP Substrate.....	51
3.4	Conclusion.....	63
4.	CONCLUSION.....	64
	REFERENCES.....	66

LIST OF TABLES

TABLES

Table 2.1: III-V material systems used for QWIP fabrication	31
---	----

LIST OF FIGURES

FIGURES

Figure 1.1 : Spectral radiant exitance of a blackbody	4
Figure 1.2: Atmospheric transmission spectrum and absorptive gas molecules. Spectrum was measured at sea level and through 6000 ft horizontal path through air containing 17 mm of precipitate water	6
Figure 1.3: Photovoltaic and photoconductive detectors	10
Figure 1.4: Illustration of the energy band profile of type II InAs/ GaInSb superlattice detector	12
Figure 2.1: Energy band diagram of QWIP structure	19
Figure 2.2: Operation principle of QWIP.....	20
Figure 2.3: (a) Conduction band diagram of Bound-to-Bound (B-B) QWIP, (b) Conduction band diagram of Bound-to-Quasibound (B-QB) QWIP, (c) Conduction band diagram of Bound-to-Continuum (B-C) QWIP, (d) Responsivity spectra of different QWIP types.....	21
Figure 2.4: 45° facet optical coupler	23
Figure 2.5: (a) Diffraction grating structure, (b) close look to the grating structure	24
Figure 2.6: Representation of corrugated QWIP structure	25
Figure 2.7: Dark current mechanisms for QWIP	26
Figure 2.8: Capture and emission processes in QWIPs	28
Figure 2.9: QWIP FPA fabrication steps	34
Figure 2.10: Schematic pixel diagram of four-band QWIP array	38
Figure 2.11: 3D view of two indium-bumps mesa structure.....	39
Figure 2.12 : Band diagram of a voltage-tunable two-color detector. The numerals without units are either energies in milli-electron volts or thicknesses in	

angstroms. The Al and In molar ratios are denoted by x and y, respectively	39
Figure 3.1: Energy band diagram of the quantum well in QWIP. E_F represents the Fermi level, E_1 is the ground state energy and E_b-E_1 is the optical activation energy	43
Figure 3.2: Noise- and photo-electrons generated by a $20 \times 20 \mu\text{m}^2$ FPA pixel operating in the wavelength range 8.0-9.0 μm looking at 240 and 290 K blackbody targets with $f/2$ aperture.	47
Figure 3.3: Gain and sensitivity of a desirable QWIP.....	48
Figure 3.4: Epilayer structure of the InP/InGaAs QWIP	50
Figure 3.5: The responsivity spectrum measurement setup	52
Figure 3.6: Responsivity spectrum of the QWIP test structures	53
Figure 3.7: Dark current and photocurrent characteristics of QWIP test structures	54
Figure 3.8: I-V characteristics of InP/InGaAs QWIP in comparison with the AlGaAs/GaAs QWIP	55
Figure 3.9: Responsivity and detectivity measurement setup	56
Figure 3.10: Peak factor calculation procedure	57
Figure 3.11: Peak responsivity values of the InP/InGaAs QWIP test structure.....	57
Figure 3.12: Noise gain and photoconductive gain values.....	58
Figure 3.13: Peak detectivity results of the test detectors with a) $f/1.5$ aperture, b) $f/2$ aperture.....	59
Figure 3.14: The peak responsivity and noise gain of the AlGaAs/GaAs QWIP.....	60
Figure 3.15: Conversion efficiency of InP/InGaAs QWIP.	61
Figure 3.16: Measured NETD values at 68 K.....	62
Figure 3.17: A thermal image recorded with the InP/InGaAs FPA at an operation temperature of 68 K and integration time of 3 ms with $f/2$ optics	63

CHAPTER 1

INTRODUCTION

All objects whose temperature is not absolute zero (0 Kelvin) emit infrared (IR) radiation. IR radiation is a form of electromagnetic radiation whose wavelength extends from 750 nm to 1000 μm in the electromagnetic spectrum. The laws of electromagnetic radiation are valid for IR radiation just like ultraviolet, visible light, radio waves and x-rays.

IR radiation was unknown until Sir William Herschel had reported his experiment with thermometers in 1800. He tried to obtain the energy distribution of the spectrum of sunlight by using a thermometer as a thermal detector in this experiment [1]. When he moved the thermometer beyond the red end of the visible spectrum, he observed a significant increase in the temperature. After that, August Ludwig Friedrich Wilhelm Seebeck discovered the thermoelectric effect in 1821 and demonstrated the first thermocouple [2]. In 1829, Leopoldo Nobili connected a number of thermocouples in series and constructed the first thermopile [2]. In 1856, Charles Piazzzi Smyth was able to detect Infrared (IR) radiation from moon with the help of a thermocouple [2]. After several years, in 1880, Samuel Pierpont Langley developed a bolometer whose principle is based on the fact that electrical resistance changes when its temperature is changed [3]. In his first bolometer, there were two thin ribbons of platinum foil as a part of a Wheatstone bridge. He improved the performance of his bolometer in the following years and achieved a 400 times more sensitive bolometer. With this bolometer, he could detect the IR radiation of a cow from a quarter of mile [3]. In 1915, William Coblentz measured the IR radiation from 110 stars by using thermopile detectors [2].

Photon detectors were developed during the 20th century. In 1971, T.W. Case developed the first IR photoconductor which is made of a substance consisting thallium and sulphur [4]. Later he added oxygen to the substance to enhance the response. In 1933, lead sulfide (PbS) was discovered by Kutzscher and it was the first practical infrared detector [5]. In the second half of the 20th century, a wide variety of new materials were developed for IR detection such as lead selenide (PbSe) and lead telluride (PbTe) [6]. Narrow bandgap semiconductors such as indium antimonide (InSb) and mercury cadmium telluride (HgCdTe) improved the IR photon detector performance. In late 1980's, research on the quantum well infrared photodetectors (QWIPs) has started. QWIP technology is improved rapidly due to the mature growth and processing techniques of the III-V materials. Today QWIPs are considered as a low cost alternative to the HgCdTe detectors. QWIP technology offers higher yield and QWIP materials show superior uniformity with respect to HgCdTe. The success in IR sensing area has lead to the commercializing of high performance photon detectors, and single pixel photoconductive detectors have been replaced by staring arrays.

1.1 Infrared Radiation

There are continually vibrating atoms in all objects around us. The vibration of these atoms generates electromagnetic waves. The higher the temperature of an object, the more frequent the vibration, and thus the higher the spectral radiant energy. As a result, every object at any given absolute temperature above 0 K emits electromagnetic radiation. The radiant power is directly related to the object's temperature leading to the term thermal radiation. The energy of emitted radiation and its wavelength is related with the following equation:

$$E = \frac{hc}{\lambda} \quad (1.1)$$

where λ is the wavelength, h is Planck's constant and c is the speed of light.

1.1.1 Blackbody Radiation

Thermal radiant emission is usually discussed in terms of the blackbody that absorbs all incident radiation at any wavelength. The energy emitted by a blackbody is the maximum theoretically possible for a given temperature since it is a perfect radiator. According to Kirchhoff's Law, the emitted radiation from a surface must be equal to the absorbed radiation by this surface at thermal equilibrium. Thus, a blackbody has an emissivity (ϵ) of 1 defined as the ratio of total exitance of a body at temperature T to the total exitance of an equivalent blackbody at the same temperature. The Planck's law states [7]

$$M(\lambda, T) = \frac{2\pi hc^2}{\lambda^5 \left[\exp\left(\frac{hc}{\lambda kT}\right) - 1 \right]} \quad (1.2)$$

where h is Planck's constant, k is Boltzmann's constant and c is the speed of light.

A series of blackbody spectra for various temperatures are shown in Figure 1.1.

As can be seen in the figure, most of the energy emitted by near room temperature objects is in the IR region. The radiant energy of a blackbody increases with temperature and the peak emittance wavelength shifts to lower wavelengths. Dependence of the peak wavelength of the blackbody radiation to object temperature is given by Wien's displacement law. The maximum radiation wavelength can be obtained by differentiating Planck's Law with respect to λ [7].

$$\lambda_{max} = \frac{2898}{T} \mu m \quad (1.3)$$

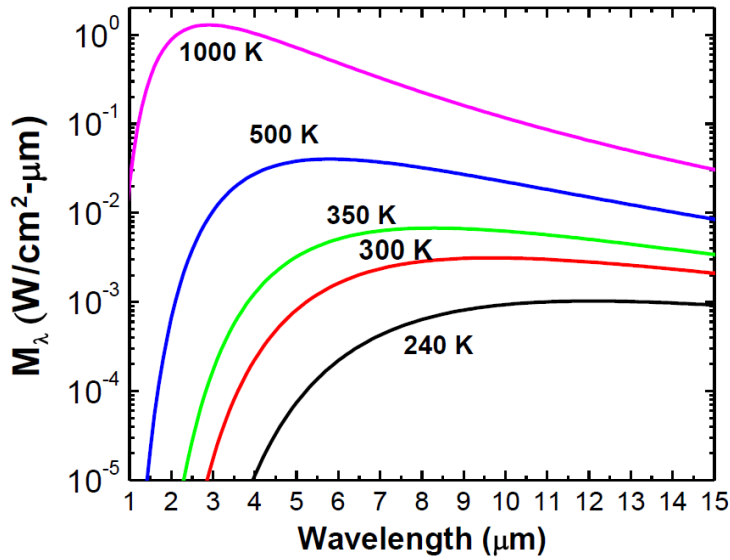


Figure 1.1 : Spectral radiant exitance of a blackbody [8]

By integrating the Planck's equation between $\lambda = 0$ and $\lambda = \infty$ total blackbody exitance can be found as follows [7]

$$M_{total}(T) = \sigma T^4 \quad (1.4)$$

where $\sigma = 5.67 \times 10^{-8} \text{ Wm}^{-2}\text{K}^{-4}$ is Stefan's constant.

1.1.2 Atmospheric Transmission

For long distance IR detection, there is a requirement of the propagation of the emitted radiation power through the atmosphere. However, the radiation power is attenuated with distance because of the fact that atmosphere is not completely transparent. Also, because atmosphere forms a background for the target, emission by the atmosphere is important in any application. The radiation emitted from the object attenuates in two different mechanisms: scattering of IR rays by atmospheric particles and absorption by the atmospheric gas molecules.

Radiation beam direction changes in scattering which is due to interaction of photons with the atmospheric molecules and aerosols. The size of aerosols like fog

and smog are larger than the radiation wavelength, so scattering of the radiation by them is independent of wavelength. Rate of scattering of photons by particles whose size is smaller than wavelength is inversely proportional to wavelength.

Absorption is the other mechanism that attenuates the radiation. Absorbing gas molecules in the atmosphere are H₂O, CO₂, CH₄, N₂O, O₃, and NH₃. Gas molecules absorb the radiation at specific wavelengths and this absorption creates the IR bands.

Figure 1.2 is a plot of the atmospheric transmission through 6000 ft as a function of wavelength. The spectrum of atmospheric transmission depends on the environmental conditions like altitude, relative humidity, climate and gas content. Specific absorption bands of water, carbon dioxide, and oxygen molecules restrict atmospheric transmission to two windows at 3–5 μm and 8–14 μm . Ozone, carbon monoxide, nitrous oxide, and methane have inconsiderable effects on the detection of the IR radiation.

As can be seen in the plot, atmosphere is relatively transparent at certain wavelength bands which are called as atmospheric transmission windows. These windows can be classified as follows:

- Near Infrared (NIR): 0.75 to 1.5 μm .
- Short Wavelength Infrared (SWIR): 1.5 to 3 μm .
- Mid Wavelength Infrared (MWIR): 3 to 5 μm .
- Long Wavelength Infrared (LWIR): 8 to 12 μm .
- Very Long Wavelength Infrared (VLWIR): 12 to 25 μm .
- Far Infrared (FIR): 25 to 1000 μm .

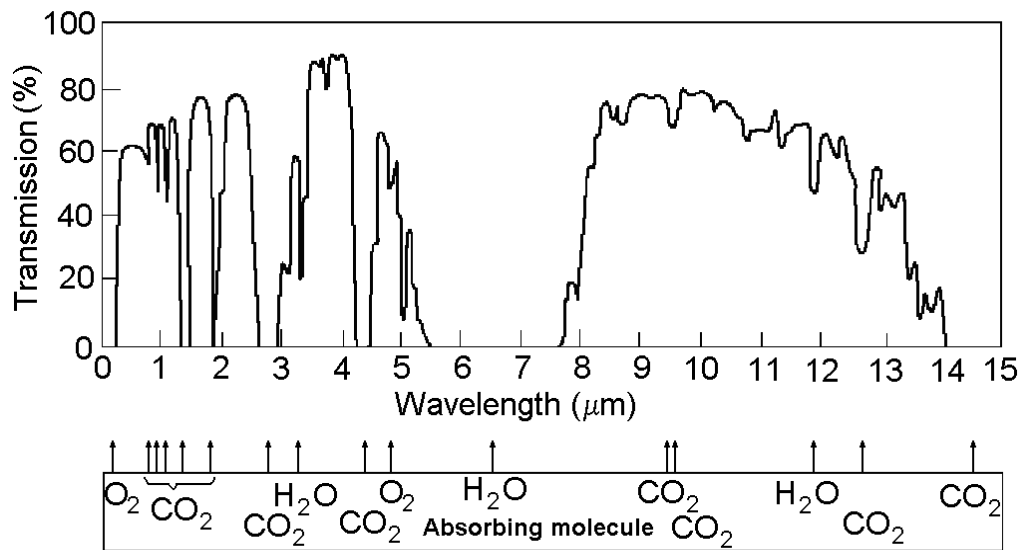


Figure 1.2: Atmospheric transmission spectrum and absorptive gas molecules. Spectrum was measured at sea level and through 6000 ft horizontal path through air containing 17 mm of precipitate water [9].

1.1.3 Choice of Infrared Band

MWIR and LWIR spectral windows are called thermal infrared bands where imaging is performed by directly detecting the photons emitted by the objects. At near room temperature, objects emit sufficient number of photons, so MWIR band and LWIR band are extremely important for thermal imaging over long distances. Also, atmosphere is highly transparent in these bands.

LWIR window is preferred for high performance because this band has higher sensitivity to objects at room temperature than MWIR [10]. Also, LWIR window is less sensitive to scattering from atmospheric molecules whose size is smaller than radiation wavelength. MWIR band also has some advantages over LWIR band. For example, MWIR band is better when contrast is more important than sensitivity because thermal contrast, which is defined as the percent change in the emitted flux for one Kelvin change in target temperature, is two times larger than that in LWIR band [10]. In addition, for hot object detection like missile and exhaust gases,

MWIR window is more appropriate choice than LWIR window. Another advantage of the MWIR band is the weaker absorption of the radiation by the water vapor in this window. It should also be noted that smaller optics can be utilized in the cameras sensing in the MWIR band, and MWIR detectors may operate at higher temperatures when compared with LWIR sensors [10]. As a result, spectral window choice depends on the target signature, atmospheric transmission, and sensor response (optics and detector).

MWIR and LWIR bands may not be fulfilling the requirements alone. Dual band/color systems are very useful in order to enhance the performance of the thermal imaging systems.

1.2 Infrared Detectors

Infrared detectors are transducers which convert the IR radiation into electric signal. There are two fundamental IR detectors classified by the physical principle of operation: thermal detectors and photon detectors.

1.2.1 Thermal Detectors

Thermal detectors respond to temperature changes generated by absorbing the electromagnetic radiation through changes in physical and electrical properties. This change is converted to electrical signals and measured by an electronic circuitry. While cryogenic cooling is not a requirement for thermal detectors, thermoelectric coolers are used for temperature stabilization. However, they suffer from low detection capability and slow response time when compared with photon detectors. On the other hand, thermal detectors are suitable for many civil applications being low cost, light and compact. Brief explanation about most common thermal detectors is given below.

Thermocouples and thermopiles: Thermocouples generate thermoelectric voltage when heated due to the Seebeck effect. For sensitive detection, there is a requirement that the thermocouple must be thermally insulated from its surroundings. For fast response, the thermocouple must be able to quickly release built up heat. Usually, the generated voltage by a single thermocouple cannot be measured accurately. Thus, multiple thermocouples are connected in series to enhance the output voltage. This structure is called thermopile.

Bolometers: Operation principle of a bolometer is based on the conductivity change of the active material due to absorption of the incident electromagnetic radiation. Usually a thin semiconductor or metal film is deposited as the absorber layer on the bolometer structure. When the thermally isolated absorbing layer is exposed to IR radiation, it heats up and so, the current passing through the detector is altered. This temperature-induced change in the conductivity can be quantified with a suitable circuitry.

Pyroelectric detectors: Pyroelectric detectors consist of a polarized material. When this material is subjected to changes in temperature, it changes polarization. When the incident IR radiation is modulated with the help of a chopper, an alternating current that can be monitored with an external amplifier flows in the external circuit connected to the opposite sides of the pyroelectric material. It is possible to estimate the intensity of the absorbed radiation from the magnitude of the measured current.

1.2.2 Photon Detectors

When photon detectors absorb infrared radiation, they convert incident photons directly into free electron-hole pairs. The generation of free carriers comes through by excitation of electrons from one energy state to another state of the semiconductor. Photon detectors require cryogenic cooling since the number of carriers thermally excited across the bandgap must be suppressed for photo-excitations to stay dominant. After the photoexcitation, free carriers are collected at

the contacts with the help of an electric field which is applied externally or built internally. Photon detectors are mainly grouped as photovoltaic and photoconductive detectors based on the generation of this electric field.

Photovoltaic detectors: In photovoltaic detectors, the excited charge carriers are collected at the contacts by a built-in electric field. Basic photovoltaic detectors are p-n junction photodiodes, Schottky barrier diodes, and metal-insulator-semiconductor (MIS) photo-capacitor devices. IR radiation impinges on the material and creates electron-hole pairs in p- and n- type region of the photodiodes by exciting the electrons. The generated electrons and holes diffuse towards the junction and are swept to the opposite side of the depletion region. As a result, photocurrent is generated in the photovoltaic detector. The photocurrent is expressed as

$$I_p = q\eta A\Phi \quad (1.5)$$

where q is the charge of electron, η is the quantum efficiency, A is the area of the photodiode, and Φ is the incident photon flux density. A photovoltaic p-n junction is shown in Figure 1.3.

Photoconductive detectors: In the photoconductive detectors, an external bias potential is applied to collect the excited carriers. The detector material can be either an intrinsic or an extrinsic semiconductor. In the case of intrinsic semiconductor, semiconductor absorbs the incident photons which have larger energies than the energy bandgap of semiconductor. Absorption excites the electrons from valence band to conduction band and increases the number of free carriers. In the case of extrinsic semiconductors, the photon energy is absorbed by the impurity, and excitation occurs from the impurity level to conduction band. Under the applied constant bias, amount of the generated current is proportional to the incident photon flux.

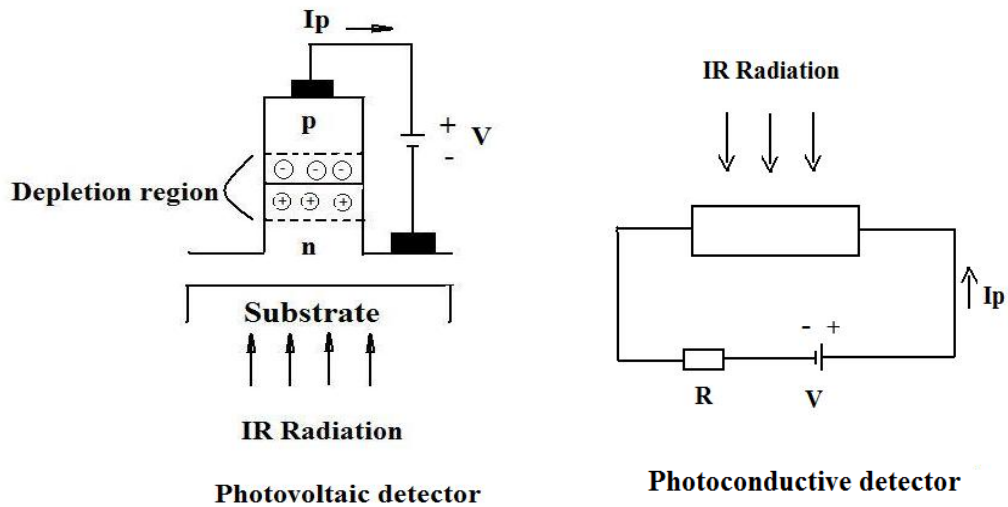


Figure 1.3: Photovoltaic and photoconductive detectors

Photon detectors may be divided into several subgroups depending on the interaction way of electrons and photons. The most important types are given below:

Intrinsic detectors: Intrinsic detectors generate free electron-hole pairs through the electron transition from valence band to conduction band in the semiconductor. Thus, the cut-off wavelength of the absorption spectrum is determined by the bandgap of the semiconductor. Most common intrinsic detector materials are PbS, PbSe, PbSnTe, HgCdTe, InGaAs, InSb, InAs and InAsSb.

Extrinsic detectors: A large bandgap semiconductor is doped with impurities in the extrinsic detector. Photoexcitation occurs between impurity levels close to the conduction band of a large bandgap semiconductor. Cut-off wavelength of the absorption spectrum is determined by the activation energy of the impurity element. Si:Ga, Ge:Hg, Si:In, and Si:Ga are widely used extrinsic materials.

Schottky diodes: Schottky diodes are different from the other detector types in terms of the absorber material. In these detectors, radiation is absorbed by the metal

element of the Schottky contact instead of the semiconductor. The most commonly used Schottky diode type is PtSi operating in the MWIR band. For long cut-off wavelength, IrSi may be utilized which requires cooling below 77 K. The incident radiation passes through transparent p-type Silicon and is absorbed in PtSi or IrSi layer. It produces hot holes which are emitted over the potential barrier into the silicon, leaving the silicide charged negatively. Then, this charge of silicide can be transferred to a CCD by the direct charge injection method. The advantage of these devices is that response depends on the characteristics of the metal which is extremely uniform. Hence, high uniformity of response is much easier to achieve. In Schottky diodes, efficiency and sensitivity are much less than that in extrinsic devices for wavelengths of a few microns since absorption is proportional to the square of the wavelength. These detectors are quite useful at very long wavelengths, beyond 100 μm .

Superlattice structures: The superlattice structure consists of two or more semiconductor materials grown in an alternating manner. The positions of the conduction bands and the valence bands with respect to each other determine the energy band diagram of this structure.

Quantum well infrared photodetectors are type I superlattices in which the bottom of the conduction band and the top of the valence band consist of the same semiconductor. There is no overlap of conduction band of one layer with the valence band of the other. In a QWIP structure, a large band gap material is combined with a smaller band gap material to form quantum wells in which the photon absorption takes place. QWIPs having the advantages of mature III-V materials can be grown with high uniformity. This high uniformity leads to the fabrication of large format focal plane arrays (FPAs) as an alternative to narrow bandgap detectors especially in LWIR and VLWIR bands.

In type II superlattice structures, there is significant overlapping of conduction and valence bands of neighboring layers. InAs/GaInSb alloy system is commonly

investigated type II Strained Layer Superlattice (SLS) detector system. This structure is illustrated in Figure 1.4. As can be seen in the figure, GaInSb valence band level is higher than InAs conduction band level forming the electron and hole minibands. Since virtual energy bandgap of the structure is lower than both InAs and GaInSb bandgaps, this structure becomes a virtual narrow bandgap detector.

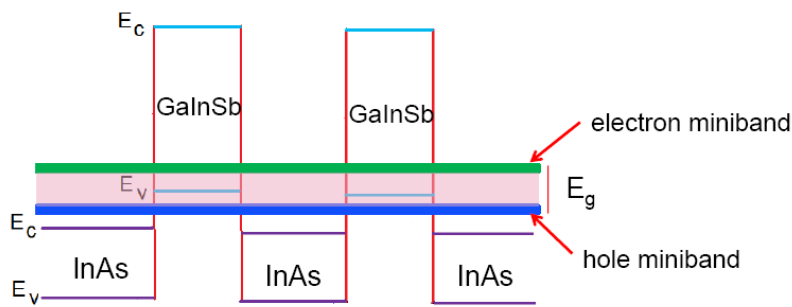


Figure 1.4: Illustration of the energy band profile of type II InAs/ GaInSb superlattice detector [11]

Type III superlattices are produced with a semi-metal layer as one of the alternating layers whose conduction and valence band symmetries are flipped. HgTe/CdTe is the commonly used material system.

1.3 Figures of Merits for Infrared Detectors

In order to assess the performance of the infrared detectors and focal plane arrays (FPAs), there are certain figures of merit which can be listed as responsivity, noise, detectivity, and noise equivalent temperature difference.

1.3.1 Responsivity

Responsivity of a detector can be defined as the amount of electrical signal produced at the output per incoming radiation power. It can be defined in terms of both voltage and current.

$$\text{Responsivity} = \frac{\text{Signal output}(A \text{ or } V)}{\text{Incoming radiation power}(W)} \quad (1.6)$$

It is possible to define the responsivity to include the incoming radiation's wavelength which is called spectral responsivity. Spectral responsivity is commonly defined in units of ampere/watts (A/W) and is expressed as [12]

$$R = q\eta g \frac{\lambda}{hc} \quad (1.7)$$

where q is the electron charge, η is the absorption quantum efficiency meaning how many electrons are excited per incoming photon, g is the photoconductive gain meaning how many electrons are collected at the external circuit for a single excited electron in the detector, λ is the detection wavelength, h is the Planck's constant, and c is the velocity of light. For photovoltaic detectors g is close to unity, whereas for photoconductive detectors, g is defined as the ratio of the average drift distance to total device length.

1.3.2 Noise

Noise can be defined as fluctuation in the signal output. It cannot be totally eliminated, but may be kept at a sufficiently low level. There are several noise mechanisms for photodetectors: Johnson noise, 1/f noise, generation-recombination (G-R) and shot noise.

Johnson (Nyquist or Thermal) Noise: Johnson noise is the fluctuation caused by the thermal motion of the charge carriers when the temperature of the semiconductor is above absolute zero. It is WHITE noise defined as the noise with

the amplitude independent of the frequency. Johnson noise current is represented as [13]

$$i_n = \sqrt{\frac{4kT\Delta f}{R}} \quad (1.8)$$

Johnson noise may appear when no bias is applied on the conductor. In QWIPs, the contribution of Johnson noise to the total noise is negligible because of the very high differential resistance of QWIPs.

Shot noise: Shot noise appears in a detector since the arrival rate of photons is random. This noise is the minimum noise level that a detector can achieve. Shot noise becomes significant at low current levels where the fluctuation is at considerable level with respect to the average current. In order to observe shot noise, there must be an applied bias on the detector. The current noise expression for shot noise is [14]

$$i_n = \sqrt{2qI\Delta f} \quad (1.9)$$

where I is the device current, Δf is the bandwidth, and q is the unit charge.

G-R noise: G-R noise is created due to the randomness of the generation-recombination processes. This noise may be due to thermal and optical generation. G-R noise current is [13]

$$i_n = \sqrt{4qIg\Delta f} \quad (1.10)$$

where I is the total current of the device, Δf is the bandwidth, g is the gain of the detector, and q is the unit charge.

The total current of the detector is equal to the sum of dark and photo currents of the detector. Both dark current and photo current generate G-R noise. The total current is expressed as

$$I = I_{photo} + I_{dark}. \quad (1.11)$$

And the photo current expression is

$$I_{photo} = q\eta g\phi_p A \quad (1.12)$$

where ϕ_p is the photon flux density and A is the device area.

If the dark current is negligible when compared to the photo current, the detector's performance is limited with the background radiation which is called background limited performance (BLIP). G-R noise current for a BLIP detector can be simplified to

$$i_n = \sqrt{4qI_{photo}g\Delta f}. \quad (1.13)$$

1/f (Pink) Noise: Although 1/f noise is observed in many different physical systems, origin of this noise is not well understood yet. 1/f noise causes fluctuations in the signal with noise spectral density inversely proportional to frequency over a wide range of frequencies limiting the low frequency detectivity. It has been shown that, for QWIPs, 1/f noise rarely limits the detector performance [15].

1.3.3 Detectivity

Detectivity is the main figure of merit characterizing normalized signal to noise performance of detectors. Detectivity is defined as the inverse of noise equivalent power (NEP) which is the minimum amount of signal power in order to obtain unity signal-to-noise ratio. For better detector performance, it needs to be maximized. NEP is expressed in terms of noise voltage or current, and can be expressed as follows;

$$NEP = \frac{i_n}{R_i} \text{ or } \frac{v_n}{R_v} \quad (1.14)$$

where R_i is the current responsivity, R_v is the voltage responsivity, i_n is the noise current, and v_n is the noise voltage.

However, NEP depends on detector area and noise measurement bandwidth and does not allow direct comparison of different detectors. Therefore, the noise term in the NEP definition is normalized to detector area and noise measurement

bandwidth. The inverse of the result is defined as specific detectivity and demonstrated as [14]

$$D^* = \frac{R_i \sqrt{A \Delta f}}{i_n} = \frac{R_v \sqrt{A \Delta f}}{v_n} \quad (1.15)$$

where A is the detector area and Δf is the measurement bandwidth. If the detector is operated under BLIP conditions, the detectivity (D^*) expression becomes [14]

$$D_{BLIP}^* = \frac{\lambda}{2hc} \sqrt{\frac{\eta}{\phi_p}}. \quad (1.16)$$

1.3.4 Noise Equivalent Temperature Difference (NETD)

Responsivity and detectivity are generally used to characterize the performance of a single pixel detector. For an imaging system, another parameter should be defined, noise equivalent temperature difference (NETD). NETD can be described as the minimum temperature difference between an object and the background required to produce an output signal equal to the noise of the system. The derivation of the NETD expression for an FPA can be found in [8]. The NETD expression is given as follows [13]

$$NETD = \frac{4(f/\#)^2 \sqrt{\Delta f}}{\sqrt{A} \int_0^\infty T(\lambda) D^*(\lambda) \frac{dM_{target}(\lambda)}{dT} d\lambda} \quad (1.17)$$

where $f/\#$ is the f-number which describes the field of view of the optical aperture, Δf is the measurement bandwidth, A is the detector area, $T(\lambda)$ is the wavelength dependent atmospheric transmission coefficient, $D^*(\lambda)$ is the spectral detectivity, and $M(\lambda)$ is the spectral radiant power of the target which is described in equation (1.2).

NETD is a measure of the thermal sensitivity of the whole imaging system. In order to obtain better thermal sensitivity, NETD values need to be smaller.

1.4 Objective of This Thesis Work

At the content of this thesis work, InP based LWIR QWIP focal plane arrays (FPAs) were investigated. A strained InP/InGaAs QWIP FPA was fabricated and characterized at the pixel and FPA levels in order to assess the feasibility and advantages of this material system as an alternative to AlGaAs/GaAs.

The main objectives of this thesis work can be summarized as follows:

- To demonstrate high performance detector arrays with relatively high quantum and conversion efficiencies under high frame rate and/or low background conditions.
- To perform a comparison between InP/ InGaAs and standard AlGaAs/GaAs material systems in terms of detector performance for high quality thermal imaging.

In this chapter of the thesis, the basics of infrared detection and the infrared detector types were mentioned.

The second chapter of the thesis includes detailed information on the operation principles and fabrication steps of QWIPs together with their comparison with HgCdTe detectors. State of the art QWIP work reported in the literature is also presented in this chapter.

In chapter three, strained InP/InGaAs LWIR QWIPs will be discussed in detail. The fabrication and characterization of InP based QWIPs will be presented along with a comparison of their performance with that of GaAs based standard QWIPs.

Finally, chapter four includes conclusions of this thesis work and the further work that can be done.

CHAPTER 2

QUANTUM WELL INFRARED PHOTODETECTORS

Quantum well infrared photodetectors (QWIPs) have become a significant member of the detector market recently because of the difficulty of the growth and processing of the intrinsic detector materials (narrow bandgap semiconductors) for especially LWIR sensing. These difficulties motivate the investigation of creating artificial narrow bandgap materials by using high bandgap semiconductors. First quantum well structure was proposed by Esaki and Sakaki by using AlGaAs/GaAs material system in 1977 [16]. After that, first QWIP is designed by Levine et al. in 1987 [17].

In this chapter, Quantum Well Infrared Photodetectors (QWIPs) will be investigated in detail.

2.1 Theory of Operation

Operation principle of a QWIP is based on the intersubband involved transitions within the same band, rather than the usual interband transition mechanism. QWIP structure has a low bandgap semiconductor well material sandwiched between two high bandgap semiconductor barrier materials. Energy levels in conduction band and valence band of this quantum well structure are quantized and discrete

subbands are produced. The structure and energy band diagram of a QWIP is illustrated in Figure 2.1.

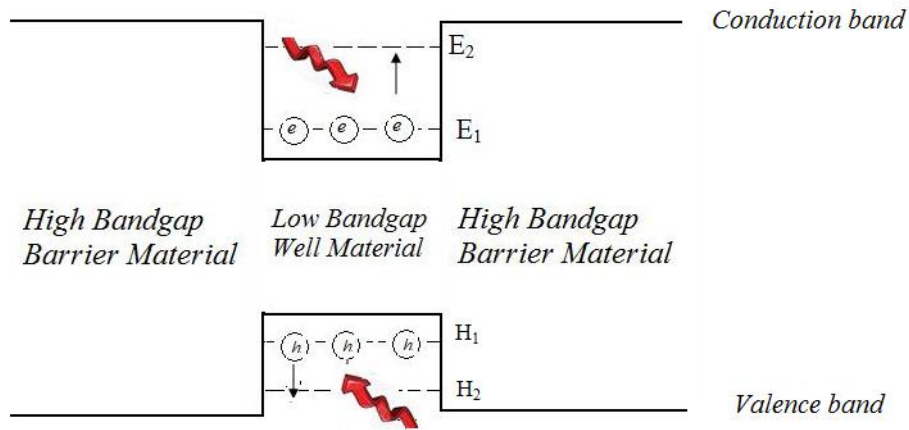


Figure 2.1: Energy band diagram of QWIP structure

The photon absorption in a QWIP takes place among these discrete energy states, from the ground state to the first excited state of the quantum well. As a result, this transition causes change in the number of mobile carriers and produces current. Each photoexcited electron either reaches the collector contact or is captured by a quantum well. QWIP operation is based on the exchange of photoelectrons between the quantum wells and contacts. Operation principle of QWIP is illustrated in Figure 2.2.

Peak absorption wavelength of a QWIP is determined by the energy difference between the ground and first excited state of the quantum well structure. Since the energy gap between energy states of the quantum well can be adjusted by controlling the compositional and dimensional parameters of the quantum well and barrier, the peak absorption wavelength can be changed with the same parameters. Energy levels in the quantum well structure can be obtained by solving the Schrödinger equation with proper boundary conditions.

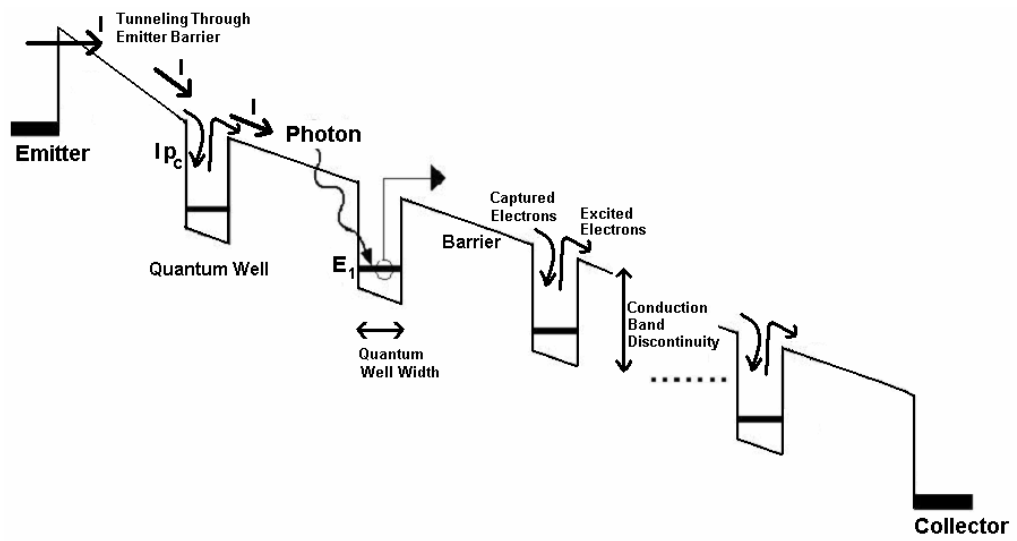
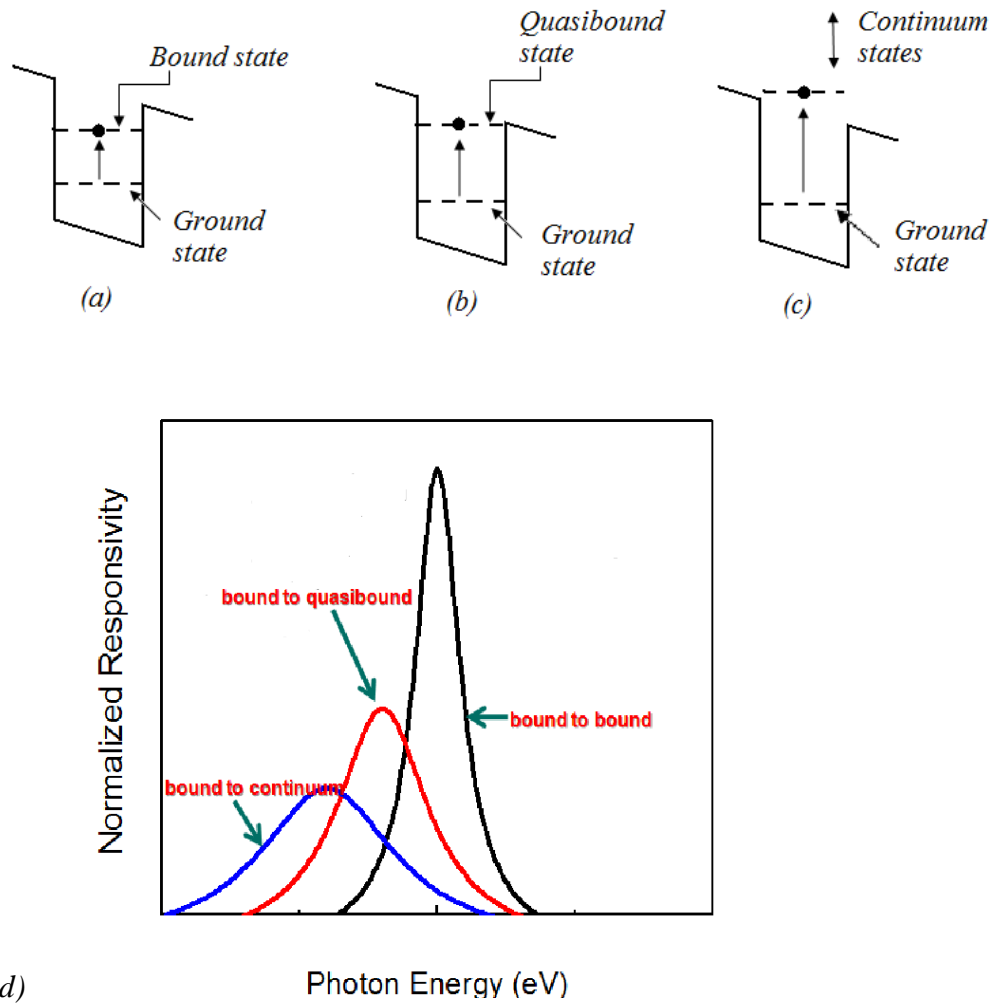


Figure 2.2: Operation principle of QWIP [18]

QWIPs are categorized according to the position of the first excited energy state level with respect to potential barrier edge. Types of QWIPs are shown in Figure 2.3.



(d)

Figure 2.3: (a) Conduction band diagram of Bound-to-Bound (B-B) QWIP, (b) Conduction band diagram of Bound-to-Quasibound (B-QB) QWIP, (c) Conduction band diagram of Bound-to-Continuum (B-C) QWIP, (d) Responsivity spectra of different QWIP types [8].

When the first excited state is below the potential barrier edge, this structure is called bound-to-bound (B-B) QWIP. In this type of QWIPs, the excited electron contributes to photocurrent by tunneling through the potential barrier. If the structure is under low applied bias, the escape probability of photoexcited electrons is low. This means that B-B QWIPs require a sufficiently high bias voltage in order to lower the potential barrier and provide thinner cross section for electrons to tunnel. On the other hand, B-B QWIPs have the highest peak quantum efficiency

due to the high oscillation strength between the ground and first excited energy states.

The bound-to-quasibound QWIP has the excited state energy located at the edge of the barrier. B-QB QWIPs need moderately high bias voltage for tunneling. The excited state is above the edge of the barrier in bound-to-continuum QWIPs in which excited electrons have high escape probability. B-C QWIPs have larger dark currents than that of the B-B QWIPs under the same bias voltage. The spectrum of B-C QWIP is broader than those of B-B and B-QB QWIPs due to more continuous excited states in the quantum well.

Total transition rate from an initial state to final states can be found by Fermi's Golden Rule as follows [12]

$$W = \frac{2\pi}{\hbar} \sum_{f,i} |M|^2 F_i (1 - F_f) \delta(E_f - E_i - \hbar\omega) \quad (2.1)$$

where F is Fermi factor and M is the matrix element which is defined as [12]

$$M = \frac{q}{m^*} \sqrt{\left(\frac{\phi\hbar}{2\varepsilon_0 n_r w c}\right)} \left[\delta_{k_{x,y}} \delta_{k'_{x,y}} \right] \sin\theta \langle \psi_{z,n'} | p_z | \psi_{z,n} \rangle. \quad (2.2)$$

In the above expression m^* is the carrier effective mass, ϕ is the photon flux, n_r is the index of refraction, w is photon frequency, and θ is the angle between the optical beam and the surface normal. By the combination of these two equations, the quantum efficiency, η , can be found as [12]

$$\eta = \frac{q^2 \hbar}{4\varepsilon_0 n_r m^* c} \frac{\sin^2\theta}{\cos\theta} n_{2D} f \delta(E_2 - E_1 - \hbar\omega) \quad (2.3)$$

where n_{2D} is the density of two dimensional electrons in the quantum well ($n_{2D} = n_{3D} L_w$), f is the oscillator strength, and θ is the angle of incidence. The quantum efficiency of the structure gives the effectiveness of the intersubband transitions, and it depends on the number of confined carriers, the oscillator strength, and the angle of incidence as seen in its expression. The angle of incident beam is significant in QWIP's operation since no absorption takes place in the case of normal incidence. Maximum quantum efficiency is obtained when the optical

electric field component is normal to the absorbing layer. In order to increase the quantum efficiency various light coupling schemes are utilized.

2.1.1 Optical Coupling

QWIPs can not absorb normal incidence radiation since light polarization must have an electric field component in the growth direction for absorption. For the simple test pixels 45° facet coupling is generally used for the correct polarization. The incident light is coupled to QWIP through 45° cut and polished edge of the substrate in this way. A 45° facet optical coupler is illustrated in Figure 2.4. Since these structures can be used only for single pixels, optical coupling schemes are required for two dimensional arrays.

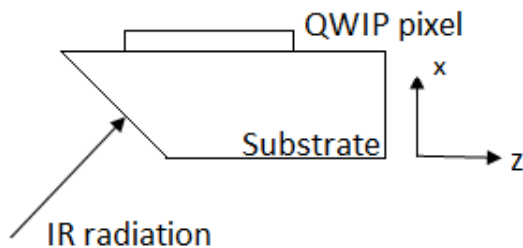


Figure 2.4: 45° facet optical coupler

Light coupling for focal plane array (FPA) pixels are utilized in the form of diffraction gratings or corrugated mesa structures. Fabricating grating structures on top of the pixel is a commonly used method to increase light coupling efficiency of QWIPs as shown in Figure 2.5. Grating structures diffract the incident light to create a parallel component to the quantum wells and increase the quantum efficiency of the device.

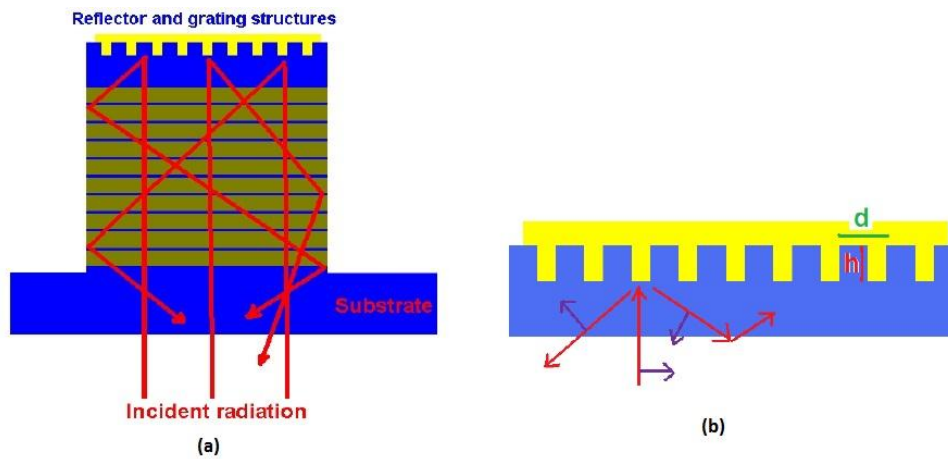


Figure 2.5: (a) Diffraction grating structure, (b) close look to the grating structure [8]

The etch depth (h) should be about one fourth of the wavelength inside the material for the maximum coupling efficiency [12].

Another coupling structure used to increase quantum efficiency in QWIPs is the corrugated QWIP (C-QWIP) structures [17]. This coupling method is based on the total internal reflection at slanted sidewalls fabricated on the active material of the QWIP structure. C-QWIP structure is represented in Figure 2.6. The reflecting sidewalls which are etched through the active quantum well layers redirect the incoming light into parallel propagation, as a result the absorption of the incoming light is maximized.

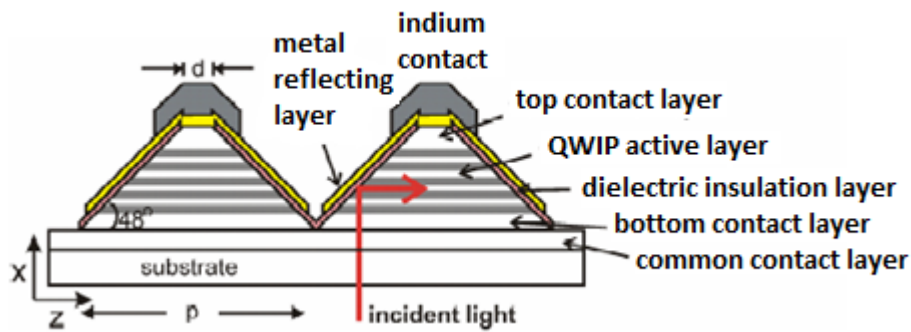


Figure 2.6: Representation of corrugated QWIP structure [19]

The C-QWIP is wavelength and size independent meaning that it preserves the natural absorption spectrum of the detector material. Therefore it is suitable for multi-color or high resolution thermal imaging.

2.1.2 Dark Current

Dark current of the detector is an important parameter because it affects the operation temperature of the device. Dark current of the QWIPs must be low enough in order to detect the incoming radiation with an acceptable signal to noise ratio (S/N). There are mainly three dark current mechanisms in QWIPs which are thermionic emission, thermally assisted tunneling, and ground state tunneling. Figure 2.7 shows these dark current mechanisms.

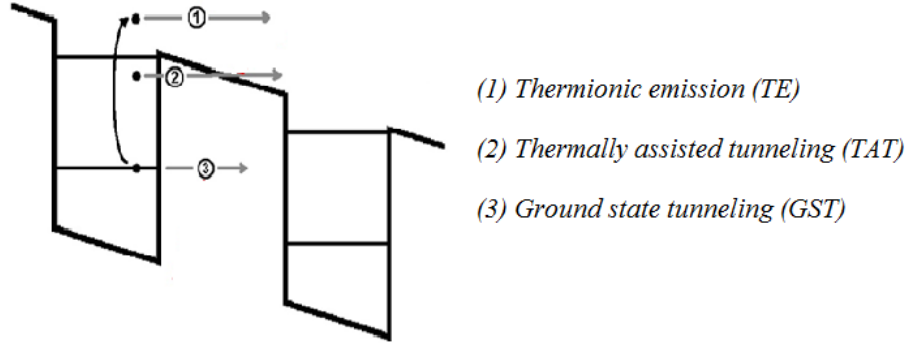


Figure 2.7: Dark current mechanisms for QWIP [8]

Thermionic emission is a major source of dark current at high temperatures (>70K) and increases exponentially with temperature. It is an intrinsic mechanism. Transport mechanism of thermally excited electrons are similar to photoexcited electrons, therefore it is difficult to suppress this dark current without sacrificing the photocurrent [20]. Elimination of the dark current is only possible when the device operates at cryogenic temperatures. Thermally assisted tunneling is a major source of dark current when the device is at medium operating temperatures (40-70 K) [20]. It may occur via trap levels in the barrier material and it can be minimized by using high quality barrier materials such as InP alloys [9]. At low temperatures (<40 K), ground state tunneling dominates the dark current. This mechanism depends weakly on temperature. In order to suppress this dark current the barrier width should be extended. Dark current can be expressed as [12]

$$I_{dark}(V) = q \times n_{thermal}(V) \times v_d(V) \times A \quad (2.4)$$

where q is the electron charge, $n_{thermal}$ is the number of thermally generated carriers, v_d is the drift velocity of electrons, and A is the detector area. The number of thermally excited carriers is given as [21]

$$n_{thermal}(V) = \frac{m^*}{\pi \hbar^2 L_p} \int_{E_1}^{\infty} f(E) T(E, V) dE \quad (2.5)$$

where m^* is electron effective mass, L_p is quantum well period, and $f(E)$ is the Fermi factor. The Fermi factor is [21]

$$f(E) = \frac{1}{\left[1 + e^{\frac{E - E_1 - E_F}{kT}}\right]} \quad (2.6)$$

E_1 is the ground state, E_F is the two dimensional Fermi level, and $T(E, V)$ is the bias dependent tunneling current transmission factor of a single barrier. Field dependent electron velocity can be expressed as [12]

$$v(V) = \mu F \sqrt{1 + \left(\frac{\mu F}{v_s}\right)^2} \quad (2.7)$$

where μ is the mobility, F is the average electric field, and v_s is saturated electron velocity.

2.1.3 Responsivity and Photoconductive Gain

QWIP current responsivity can be expressed as [21]

$$R_i = q\eta g \frac{\lambda}{hc} = q\eta_a p_e g \frac{\lambda}{hc} \quad (2.8)$$

where η_a is the absorption quantum efficiency and p_e is the escape probability of a photoexcited electron from quantum well into conduction band without recapturing which is defined as [12]

$$p_e = \frac{1}{1 + \frac{\tau_e}{\tau_r}} \quad (2.9)$$

In the above expression τ_e is the time required for a carrier to escape from the vicinity of the well, and τ_r is the carrier recapture time. The escape time depends exponentially on the electric field while the recapture time is independent of field. For high responsivity the escape probability must approach to unity.

Capture and emission processes in QWIPs are shown in Figure 2.8. Capture probability (p_c) is the probability of an electron to be captured by a well while it is flowing through the device.

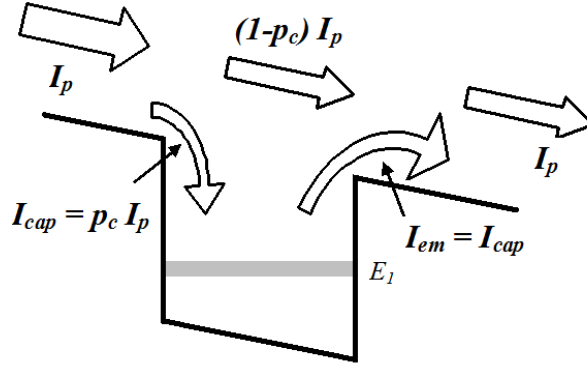


Figure 2.8: Capture and emission processes in QWIPs [9]

The current continuity requires that the current captured by the quantum well must be identical to the current emitted by the same well. If we assume that the device current is dominated by the photo current, the current continuity equation is [21]

$$I_p = (1 - p_c)I_p + I_{em} \quad (2.10)$$

and [21]

$$I_{em} = q\phi\eta_1 = p_c I_p \quad (2.11)$$

where ϕ is the photon flux and η_1 is the quantum efficiency of a single well.

The photocurrent generated by unit area of the detector is [21]

$$I_p = q\phi\eta g. \quad (2.12)$$

η is the total quantum efficiency of the wells which is given by

$$\eta = N_w \eta_1 \quad (2.13)$$

where N_w is the total number of quantum wells. Then, the photoconductive gain of the QWIP is found as [21]

$$g = \frac{1}{p_c N_w} \quad (2.14)$$

The photoconductive gain can also be given as [21]

$$g = \frac{\tau_L}{\tau_t} = \frac{v_{drift}\tau_L}{v_{drift}\tau_t} = \frac{L_{drift}}{L} \quad (2.15)$$

where τ_L is the photoexcited electron lifetime, τ_t is the electron transit time through the QWIP structure, v_{drift} is the electron drift velocity, L_{drift} is the photoexcited electron drift distance, and L is the total device length. In other words, photoconductive gain can be described as the ratio of the electron's drift distance to the device length. Longer electron drift distance means larger optical gain, hence greater responsivity.

2.1.4 Noise

1/f noise and Johnson noise can be neglected in QWIPs under typical operating conditions. The dominant noise mechanism in QWIPs is the G-R noise which is due to fluctuations in the device current as a result of both dark current and photocurrent generation mechanisms. The total noise current is expressed as

$$i_n = \sqrt{4q(I_{dark} + I_{photo})g\Delta f} \quad (2.16)$$

where $I_{dark} = qn_{thermal}v_{drift}A$, $I_{photo} = q\eta g\phi_b A$, and $g = \frac{v_{drift}\tau_L}{L}$.

G-R current noise expression under dark current limited conditions (at low illumination level or high detector temperature) can be written as [12]

$$i_n = \sqrt{4qI_{dark}g\Delta f} = \sqrt{4q^2n_{thermal}v_{drift}g\Delta f} \quad (2.17)$$

2.1.5 Detectivity

In detectivity calculation there are various noise mechanisms need to be considered. However G-R noise alone can determine the standard QWIP performance. Under dark current limited conditions, the detectivity expression of the QWIP is [12]

$$D^*_{dark} = \frac{\eta}{2hc/\lambda} \sqrt{\frac{\tau_L}{n_{thermal}L}} \quad (2.18)$$

If the detector is operating at BLIP condition, the detectivity becomes [21]

$$D^*_{BLIP} = \frac{\lambda}{2hc} \sqrt{\frac{\eta}{\phi_b}} \quad (2.19)$$

2.2 Material Systems for QWIPs

QWIP focal plane arrays can be fabricated by using different material systems with III-V semiconductors. This is an advantage of QWIP technology over other detector systems due to low cost of mature III-V semiconductors.

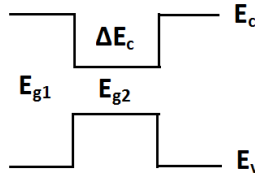
Commonly used material systems for QWIPs are GaAs based. $\text{Al}_x\text{Ga}_{1-x}\text{As}/\text{GaAs}$ material system is generally used for LWIR detection. For MWIR band detection this system is not utilized because an Al mole fraction higher than 0.45 is needed for sensing in this band. With this high Al mole fraction in the barrier material, energy crossing of the Γ and X valleys decreases the thermal activation energy of the ground state electrons and increases the dark current [22]. For efficient MWIR sensing, $\text{In}_y\text{Ga}_{1-y}\text{As}$ material can be utilized as a quantum well material while keeping the Al mole fraction less than 0.45 in the barriers. However, strain is introduced into the layer due to the lattice mismatch between $\text{In}_y\text{Ga}_{1-y}\text{As}$ material and barrier material.

$\text{InP}/\text{In}_x\text{Ga}_{1-x}\text{As}$ material system can also be used for LWIR QWIPs. InP is the barrier material and $\text{In}_{0.53}\text{Ga}_{0.47}\text{As}$ is the quantum well material which is lattice matched to InP. This system has a cut-off wavelength around $8.5\ \mu\text{m}$ which is too short for most LWIR applications [23]. In order to obtain longer cut-off wavelength, InGaAsP can be used as a well material instead of $\text{In}_{0.53}\text{Ga}_{0.47}\text{As}$. Another method for lengthening the cut-off is using lattice mismatched InGaAs material.

The significant advantage of InP based systems is their high photoconductive gain due to large energy spacing between Γ and L valleys in the barrier material [24]. This higher gain leads up higher responsivity than that of GaAs based systems. For MWIR detection, $\text{In}_{0.52}\text{Al}_{0.48}\text{As} / \text{In}_{0.53}\text{Ga}_{0.47}\text{As}$ material system can be used in which $\text{In}_{0.52}\text{Al}_{0.48}\text{As}$ is the barrier material. In MWIR region, InP based system provides a lattice matched alternative to strained GaAs based counterparts. In the following table, mature III-V material systems for QWIPs are given.

Table 2.1: III-V material systems used for QWIP fabrication [8].

Material System	E_{g1} (eV)	E_{g2} (eV)	ΔE_c (eV)	Comments
$\text{Al}_x\text{Ga}_{1-x}\text{As}/\text{GaAs}$	Variable	1.43	Variable	Used for LWIR QWIPs, ΔE_c is insufficient for MWIR QWIPs with acceptable x
$\text{Al}_x\text{Ga}_{1-x}\text{As}/\text{In}_y\text{Ga}_{1-y}\text{As}$	Variable	Variable	Variable	Used for MWIR QWIPs
$\text{InP}/\text{In}_{0.53}\text{Ga}_{0.47}\text{As}$	1.35	0.75	0.25	Used for LWIR QWIPs, high R, cut off wavelength adjustable with strain
$\text{Al}_{0.52}\text{In}_{0.48}\text{As}/\text{In}_{0.53}\text{Ga}_{0.47}\text{As}$	1.45	0.75	0.5	Used for MWIR QWIPs



2.3 Fabrication of QWIP Focal Plane Arrays

QWIP FPA fabrication starts with the epitaxial growth of the material system. Commonly used QWIP growth technologies are Molecular Beam Epitaxy (MBE) and Metal Organic Vapor Deposition (MOCVD). MBE technique was used in this study. It was developed in order to grow high purity epitaxial layers in the early 1970s [25]. MBE system has precise control over layer thickness, doping profile, and composition. Since MBE uses solid sources instead of gaseous one, it is safer than MOCVD.

A typical MBE system consists of three chambers; loading chamber, buffer and the growth chamber. The loading chamber is used for loading the substrates without venting the ultra-high vacuum (UHV) environment. The buffer is used for pretreatment of the substrate surface, and the growth chamber is for growing epilayers. Growth chamber includes effusion cells, substrate holder, in-situ characterization tools, system monitoring equipments and pumping systems. Effusion cells contain the source materials which are loaded into pyrolytic boron nitride (PBN) crucibles. The reason to choose PBN is the low rate of gas desorption from this material. There are shutters in front of the cells to interrupt the fluxes from the cells immediately if needed. To obtain high-purity layers, it is critical that the material sources be extremely pure and that the entire process be done in an UHV environment [26]. UHV environment is obtained by several pumps installed on the system and cryopanel cooled with liquid nitrogen. UHV environment allows installing several in-situ characterization tools to the system. Reflection High Energy Electron Diffraction (RHEED) which is a technique used to characterize the surface of crystalline materials is one of them. The phase transitions, the growth rate, and the strain can be monitored by RHEED during the growth. In addition to RHEED, a residual gas analyzer who measures the partial pressures of the molecules inside the chamber and a pyrometer for measuring the substrate temperature can be mounted on the system.

Before starting the growth process, the effusion cells are heated from stand by temperatures to growth temperatures. After the heating process, the substrate is loaded into the reactor. Then, the substrate is passed to the buffer chamber by a transport mechanism. After the pretreatment of the substrate surface, the substrate is loaded into growth chamber with all the shutters closed. Growth procedure starts with heating of the substrate to remove the surface oxide for the growths on GaAs and InP substrates. Then, substrate is taken to the growth temperature. The effusion cell shutters and the substrate shutter are opened and the source materials are deposited on the substrate. When the growth is complete, all the shutters are closed and the substrate is cooled.

After the epitaxial growth and characterization of the wafer, QWIP FPA fabrication process starts. First of all, alignment marks on the sample are deposited after UV photolithography step. Then, diffraction gratings are formed by using photolithography and etching processes. Afterwards, mesa etch is done by either wet or dry etching techniques in order to isolate the pixels from each other. Deposition of the ohmic contact metals is done by thermal evaporation and the sample is annealed at high temperatures for diffusion of the ohmic contact metals. In order to be able to increase the low quantum efficiency of QWIP structure, a reflecting metal layer is deposited on top of the mesa structures. As a next step, passivation layer is constructed for neutralizing the surface states. Passivation layer is patterned and etched to obtain an opening for the metal contacts for each mesa. Following this step, under bump metallization (UBM) is evaporated as a sticky surface for indium bumps which connect the detector and read-out integrated-circuit (ROIC). Indium bump deposition is an important step in the fabrication process and is achieved with the help of an e-beam evaporation system. After all, the sample is diced and flip-chip bonded to the Si based ROIC. With the aim of increasing the mechanical strength of the FPA and ROIC hybrid, an underfill epoxy is injected between the detector array and the ROIC. Substrate thinning process is needed because there is a mismatch of thermal expansion coefficient between the silicon ROIC and detector material. In order to avoid the cracking of the hybrid during the thermal cycles and reduce the optical crosstalk between the pixels, the substrate is thinned to leave approximately 10 micrometers of bulk material. Finally, anti reflection material is coated through the FPA substrate. The fabrication steps are summarized in Figure 2.9.

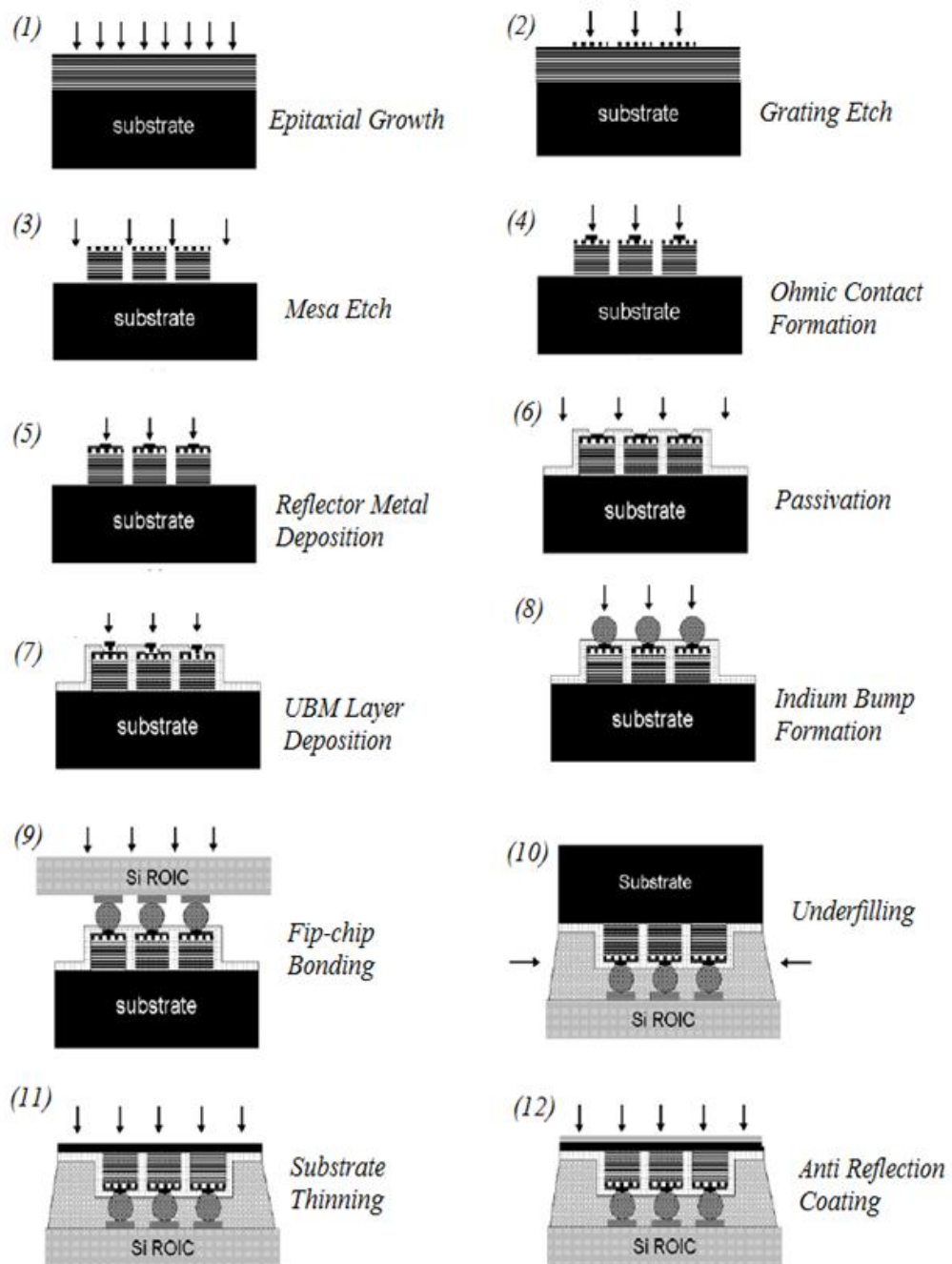


Figure 2.9: QWIP FPA fabrication steps [9]

2.4 QWIP versus HgCdTe Photodetectors

HgCdTe detectors have been one of the most common IR sensors operating since 1959. QWIP has become a successful alternative to MCT technology especially in the LWIR band after rapid progress in QWIP technology since 1985. MCT detector technology is relatively mature in the MWIR region.

MCT photodetectors have large optical absorption which is independent of light polarization. As a result, they have high quantum efficiency around 70% without anti reflection (AR) coating and 90% with AR coating [27]. QWIPs have lower quantum efficiency than MCT detectors due to the lack of normal incidence absorption in these structures. Due to lower quantum efficiency, operation temperature of QWIPs is also lower than MCT detectors. If single pixel level comparison is considered, MCT devices show better performance than QWIPs. On the other hand, FPA performance strongly depends on the material uniformity as well. Non-uniform growth of MCT is the basic limitation of this material for FPA fabrication. Non-uniformity arises from the strong Cd mole fraction dependency of the bandgap of MCT especially in LWIR and VLWIR region. Since the substrate material (CdZnTe) is expensive and unavailable in large sizes, production cost of MCT detector is high. On the contrary, QWIPs have the advantages of consisting of the mature III-V semiconductors. QWIP material can be grown uniformly in large areas and QWIP FPAs can be fabricated in large format. The maturity of QWIP materials leading to high yield decreases the fabrication cost of QWIP FPAs.

The recent studies in QWIP technology is toward improving the quantum efficiency by utilizing new optical coupling structures such as the corrugated pixel.

2.5 State of the Art in QWIPs

Due to the rapid development in QWIP device technology 1024x1024 QWIP FPAs are now commercially available. Recent studies intend to increase the sensitivity of devices as well as increasing the array formats. In addition, multi-color structures are studied in recent years.

1024x1024 QWIP FPAs which are operated in the LWIR and MWIR bands were demonstrated by Gunapala et.al [28]. In this work, standard AlGaAs/GaAs and AlGaAs/GaAs/InGaAs material systems were used for LWIR and MWIR regions for FPA fabrication. MWIR detector utilized coupled quantum wells which consisted of two wells of 40 Å separated by 400 Å AlGaAs barrier in order to increase the responsivity spectrum broadness. One well was composed of 10 Å GaAs, 20 Å InGaAs, and 10 Å GaAs layers. The FPA pixel size was 17.5 μm x 17.5 μm and pitch size was 19 μm. MWIR FPA yielded a mean NETD of 17 mK with f/2.5 optics, 60ms integration time and 300 K background at 90 K operating temperature [28]. The operability of FPA was 99.95%. Besides very good performance of the MWIR device, LWIR QWIP FPA also showed satisfying performance. LWIR QWIP with a cut off wavelength of 8.8 μm yielded peak detectivity of 1×10^{11} cmHz^{1/2}/W. LWIR FPA yielded NETD of 16 mK with f/2.5 optics and 29 ms integration time at 72 K operating temperature [28]. The operability of FPA was 99.98% for 300 K background.

Multi-color/band QWIP FPAs have recently been investigated by several groups. Mainly three approaches are used for the fabrication of the multi-color/band FPAs. In the three-contact FPA approach there are three indium bumps for each pixel instead of one. It provides simultaneous detection of different colors. However, large format arrays are not possible with this approach. The other technique is fabricating spatially shared FPA. The spatially selected pixels fabricated to detect one wavelength facilitate simultaneous integration of the signals in different bands. Low fill factor and lower resolution are the drawbacks of this approach. Another

approach is forming voltage tunable FPAs. In this approach the detection wavelength can be adjusted by changing the applied bias. Although this approach does not allow simultaneous detection, it provides large format, high yield, and low cost dual-band FPA fabrication.

Commonly studied dual band devices are LWIR/MWIR FPAs. There is limited number of work on MWIR/MWIR and LWIR/LWIR devices. Mid-format (256x256) MWIR/MWIR, MWIR/LWIR and LWIR/LWIR QWIP FPAs with the three-contact approach were fabricated by Sundaram et.al. [29]. MWIR/MWIR array with 4 μm and 4.7 μm peak wavelengths showed NETDs of 41 mK at 85 K operating temperature and 32 mK at 90 K for 8 ms and 10 ms integration times and $f/3$ optics [29]. LWIR/LWIR multicolor FPA with 8 μm and 11 μm peak wavelength yielded NETDs of 22 mK and 15 mK for 100 Hz frame rate and $f/3$ optics at 40 K [29]. NETDs better than 35 mK in both bands were obtained for the MWIR/LWIR FPA with $f/2$ optics, 100 Hz frame rate and 65 K detector temperature. The operability of the FPA was around 97% [29].

In 2003, 640x512 format four-band QWIP FPA based on the InGaAs/GaAs/AlGaAs material system was reported by Bandara et.al. [30]. This four band FPA was constructed according to spatially shared array approach and consisted of four different IR bands sensitive to 4-5.5 μm , 8.5-10 μm , 10-12 μm , and 13-15.5 μm , respectively. Each band has the format of 640x128. Schematic pixel diagram of the four-band QWIP array is given in Figure 2.10. Since the operation temperature of the device is determined by the longest wavelength, the device has been operated at 45 K. NETD values of the device was obtained as 21.4, 45.2, 13.5, 44.6 mK for 4–5.5, 8.5–10, 10–12, and 13–15.5 μm spectral bands, respectively at 40 K [30]. The operability of the FPA was 99.9%.

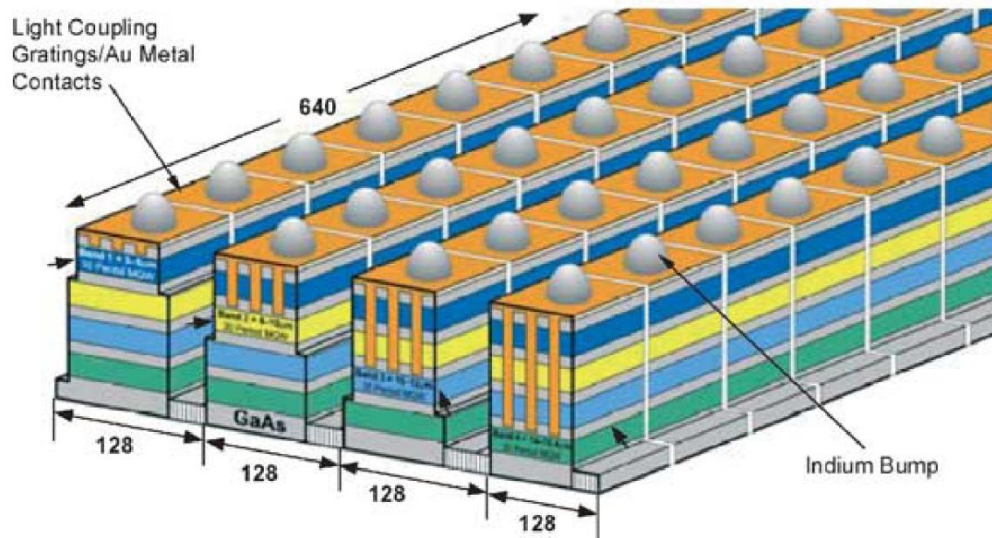


Figure 2.10: Schematic pixel diagram of four-band QWIP array [30]

Gunapala et.al. demonstrated a megapixel (1024x1024) dual-band QWIP FPA [31]. Standard AlGaAs/InGaAs/GaAs material systems were utilized. FPA was fabricated with co-registered pixels with two indium bumps per pixel approach instead of conventional three indium bumps. The illustration of this approach is given in the Figure 2.11. In order to broaden the spectral response, coupled InGaAs/AlGaAs quantum wells were used in the MWIR part. LWIR part was constructed with the standard AlGaAs/GaAs material system. Full width at half maximum (FWHM) of the MWIR part extends from 4.4 μm to 5.1 μm and that of the LWIR detector covers 7.8-8.8 μm range. MWIR part is under BLIP condition with $f/2.5$ optics up to -1 V bias and exhibits a peak detectivity of $4 \times 10^{11} \text{ cmHz}^{1/2}/\text{W}$ at 90 K FPA temperature. LWIR stack is BLIP at 72 K temperature with -1 V bias and $f/2.5$ optics and gives peak detectivity of $1 \times 10^{11} \text{ cmHz}^{1/2}/\text{W}$ at 70 K temperature. The measured NETD values were 27 mK for MWIR stack and 40 mK for LWIR stack at 70 K operating temperature. The operability of the FPA was approximately 90% due to the complex fabrication process.

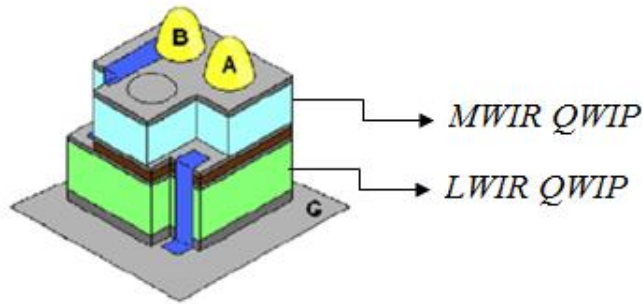


Figure 2.11: 3D view of the two-indium bump mesa structure [31]

Choi et.al. demonstrated a 256×256 voltage-tunable two-color corrugated QWIP (C-QWIP) FPA [32]. Spectral tuning mechanism of the structure was based on photocurrent asymmetry in a double- superlattice quantum well structure. In this structure, two quantum well stacks with thin barriers were separated by a graded barrier in the middle as shown in Figure 2.12. They obtained high quantum efficiencies due to the corrugated light coupling structure: 24% for the MWIR band and 26% for the LWIR band without AR coating. At 50 K operating temperature the measured NETD values were 27 mK at 33-ms integration time for the MWIR and 90 mK at 2 ms for the LWIR with $f/2.44$ optics. The NETD operability values are 98.4% and 95.9%, respectively.

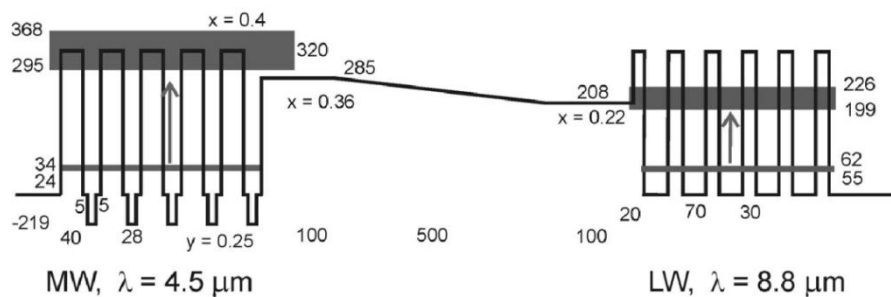


Figure 2.12 : Band diagram of a voltage-tunable two-color detector. The numerals without units are either energies in milli-electron volts or thicknesses in angstroms. The Al and In molar ratios are denoted by x and y , respectively [32].

Recently, Arslan et. al. have demonstrated voltage tunable two-color 640x512 MWIR/LWIR FPAs [33]. They implemented the dual band detectors according to the conventional FPA fabrication process requiring only one indium bump for each pixel. The spectral response of a two-stack structure can be shifted between MWIR and LWIR bands by adjusting the applied bias. This device with 5.1 and 8.9 μm cut off wavelengths provided NETD values of 14 and 31 mK with f/1.5 optics for MWIR and LWIR bands, respectively.

In addition to GaAs based QWIP research, there are some studies reported on InP based QWIPs in the literature. LWIR InP/InGaAs QWIPs grown by metal organic molecular beam epitaxy (MOMBE) were first demonstrated by Gunapala et. al. in 1991 [34]. They reported much larger responsivity values for these QWIPs than that of AlGaAs–GaAs QWIPs under large bias voltages. A similar observation was reported by Andersson et al. on InP/InGaAs QWIPs grown by metal organic vapor phase epitaxy (MOVPE) [35]. Large gain and responsivity in InP/InGaAs QWIPs were also reported by other groups [36] [37] [38] and the first mid format (256x256) InP/InGaAs QWIP FPA was reported by Jiang et. al. using metal organic chemical vapor deposition (MOCVD) grown material. The first large format (640x512) InP/InGaAs QWIP FPA was reported by Celtek et. al. [23] and InP/InGaAsP QWIP FPA was reported by Ozer et. al. [39] with desirable thermal imaging performance.

Even though InP/InGaAs QWIPs show significant advantages, they have a disadvantage which is the lack of flexibility in adjusting the peak detection wavelength by altering the barrier/well material composition in the lattice matched structure. In this structure, cut-off wavelength is limited around 8.5 μm . On the other hand, Gusakov et. al. showed that this limitation can be overcome by utilizing the strain as an additional design parameter [40]. The operating wavelength can be extended up to 11 μm by this technique. Eker et. al. demonstrated large format (640x512) strained InP/InGaAs QWIP FPA with 9.7 μm cut-off wavelength for high speed thermal imaging [41]. Gunapala et. al. reported that it is also possible to

extend the cut-off wavelength to 9 μm by using InGaAsP instead of InGaAs as the quantum well material [42]. This is also reported by Ozer et. al. [39].

Besides InP based LWIR QWIPs, MWIR AlInAs/InGaAs QWIPs on InP substrate also have some advantages over standard GaAs based QWIPs. AlInAs/InGaAs MWIR QWIPs are lattice matched to the InP substrate and they become an alternative to the strained AlGaAs/InGaAs material systems in the MWIR band. However, there is limited amount of study about AlInAs/InGaAs QWIPs in the literature. The capability of the AlInAs/InGaAs system for MWIR QWIPs was first investigated by Levine et. al. [43]. This QWIP structure was a B-B QWIP with an absorption peak wavelength of 4.4 μm and $\Delta\lambda/\lambda_p \sim 7\%$. The broader absorption linewidth (93 meV) was obtained by Hasnain et. al. by decreasing the quantum well width [44]. The detectors yielded 25 mA/W peak responsivity at 4 μm peak wavelength. Lately, Fathimulla et al reported a 320x250 MWIR QWIP FPA on InP substrate with NETD of 90 mK and 88% operability [45]. Maximum QWIP responsivity reported with this material was 300 mA/W. Recently, the first large format (640x512) AlInAs/InGaAs QWIP FPA with 4.6 μm cut-off wavelength was reported by Ozer et. al. [46]. NETD of the FPA was reported as low as 23 mK with f/1.5 optics at 105 K detector temperature with 99.6 % operability. AlInAs/InGaAs material system also shows the potential of utilization in dual/multi band QWIP FPA due to the possibility of growth with the InP/InGaAsP system under completely lattice matched conditions.

QWIP fundamentals, comparison of QWIPs with MCT detector technologies and QWIP state of the art have been presented in this chapter. The next chapter will present InP based LWIR QWIP technology.

CHAPTER 3

InP BASED LWIR QWIP TECHNOLOGY

Although AlGaAs/GaAs material system is generally accepted as a standard in LWIR QWIP technology, InP/InGaAs system offers similar maturity level while providing some advantages over AlGaAs/GaAs. In this chapter, InP based QWIP structures are investigated in detail.

3.1 Advantages of InP based QWIPs

The low quantum efficiency and low gain of the standard AlGaAs/GaAs QWIPs is the biggest bottleneck of this material system for employment of these QWIPs in high performance thermal imaging. In general, InP/InGaAs QWIPs offer higher responsivity due to higher gain. The need for high quantum efficiency and gain comes from the requirements for the utilization of QWIPs for low integration time (high frame rate) and/or low background applications. Actually, standard QWIP FPAs can show excellent thermal imaging performance when the integration time is long enough. However, for low integration times and /or low backgrounds InP/InGaAs QWIPs are expected to show better imaging performance.

The absorption quantum efficiency linearly depends on the density of two dimensional electrons in the quantum well (n_{2D}) and it is inversely proportional to the effective mass of the quantum well material as shown in Equation 2.3. GaAs quantum wells used in GaAs based QWIPs have an electron effective mass of $0.067 m_0$ [47], whereas InGaAs quantum wells used in InP based QWIPs have $0.041 m_0$

[48]. In this case, the quantum efficiency of InP/InGaAs QWIPs is expected to be 1.63 times higher than that of AlGaAs/GaAs QWIPs for the same n_{2D} . On the other hand, InP/InGaAs QWIPs are expected to have higher dark current at the same doping density due to the higher position of the Fermi level according to the following equation relating the n_{2D} to E_F and m^* [12]

$$n_{2D} = \frac{m^*kT}{\pi\hbar^2} \ln \left(1 + e^{\frac{E_F}{kT}} \right). \quad (3.1)$$

Let's look at the comparison between InP/InGaAs QWIP and AlGaAs/GaAs QWIP in terms of photocurrent and dark current [11]. Let's assume that both QWIPs have 50 Å thick quantum wells, the same optical activation energy, $E_b - E_1$, and the same doping level which is the optimum doping level for highest detectivity in AlGaAs/GaAs QWIPs ($\sim 4 \times 10^{17} \text{ cm}^{-3}$, $n_{2D} = 2 \times 10^{11} \text{ cm}^{-2}$) [11]. Also, all the other parameters are assumed to be similar in the two QWIPs. Since these two QWIPs have the same doping level, it is expected that Fermi level of InP/InGaAs QWIP is located at a higher level than that of AlGaAs/GaAs QWIP according to Eq 3.1. The differences between the Fermi level (E_F) and the ground state (E_1) are 5.33 and 10.93 meV in AlGaAs/GaAs and InP/In_{0.53}Ga_{0.47}As QWIPs, respectively [11].

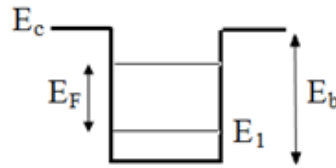


Figure 3.1: Energy band diagram of the quantum well in QWIP. E_F represents the Fermi level, E_1 is the ground state energy and $E_b - E_1$ is the optical activation energy [8].

Assuming that the quantum efficiency of the InP based QWIP is 1.63 higher than the GaAs based QWIP, the photocurrents of two QWIPs can be related as the following [11]

$$I_{p_{InP}} = 1.63 I_{p_{GaAs}}. \quad (3.2)$$

The dark current ratio of InP and GaAs based QWIPs can be determined by using the temperature dependent dark current expression [21]

$$I_d \propto T m^* e^{-\frac{E_b - E_1 - E_F}{kT}} \quad (3.3)$$

and calculated as [11]

$$\frac{I_{d_{InP}}}{I_{d_{GaAs}}} = \frac{m^*_{InP} e^{\frac{E_{F_{InP}}}{kT}}}{m^*_{GaAs} e^{\frac{E_{F_{GaAs}}}{kT}}} = \frac{m^*_{InP}}{m^*_{GaAs}} \frac{e^{\frac{E_{F_{InP}}}{kT}}}{e^{\frac{E_{F_{GaAs}}}{kT}}} = \frac{1}{1.63} e^{0.61 \frac{E_{F_{GaAs}}}{kT}} = 1.67. \quad (3.4)$$

Finally, the photocurrent and dark current ratio is found to be similar for the two QWIPs.

$$\frac{(I_p/I_d)_{InP}}{(I_p/I_d)_{GaAs}} = \frac{1.63}{1.67} \approx 1. \quad (3.5)$$

This result shows that InP based QWIP has 60% higher quantum efficiency than GaAs based one for the same doping level by offering the same I_p/I_d ratio at the same operating temperature.

Another point of view is that the dark current of the InP based QWIPs will be lower than that of the GaAs based QWIPs when the same quantum efficiency is targeted. InP based QWIPs can be doped at a density 1.63 times lower for the same quantum efficiency [11]. Then the dark current ratio can be calculated as

$$\frac{I_{d_{InP}}}{I_{d_{GaAs}}} = \frac{m^*_{InP} e^{\frac{E_{F_{InP}}}{kT}}}{m^*_{GaAs} e^{\frac{E_{F_{GaAs}}}{kT}}} = \frac{1}{1.63} \frac{2.49}{2.59} = 0.59 \quad (3.6)$$

for 65 K operating temperature [11].

If (I_p/I_d) is considered for the same quantum efficiency, in InP based QWIP it is 1.7 times larger than in GaAs based QWIP since the photocurrents are at the same level in this case. This higher ratio results in roughly 3 K higher BLIP temperature in InP based QWIP if the peak responsivity wavelength is approximately 9 μm [11].

Higher responsivity which arises from the larger gain of the InP barrier material is the another advantage of the InP/InGaAs QWIPs. Γ -L energy spacing in the InP barrier material is larger than AlGaAs barrier material. This higher energy difference causes the conduction of the photoelectrons with higher kinetic energy within the barrier and lower capture probability. Larger drift distance in InP based QWIPs can be attributed either to larger photo excited carrier lifetime due to lower capture probability or to the better transport properties of the binary InP. As a result, larger drift distance gives higher device gain.

The drift distance and gain in InP/InGaAs QWIPs saturate at a value significantly larger than that achievable with AlGaAs/GaAs. Therefore larger device gain values can be achieved without saturation due to bias adjustable gain of the InP/InGaAs QWIPs.

Although larger gain provides a higher responsivity, the detectivity of a BLIP detector is independent of the gain due to the similar dependency of signal and noise levels of the device on the gain. In this sense, the temporal noise equivalent temperature difference (NETD) of the BLIP detector does not depend on the device gain as long as the capacity of the read out integrated circuit (ROIC) capacitors is unlimited. The expression for NETD of a BLIP detector is [49]

$$NETD = \frac{kT^2}{h\nu} \sqrt{\frac{2g}{N_s}} \quad (3.7)$$

where $h\nu$ is the photon energy and N_s is the collected photoelectrons. N_s depends on the photoconductive gain (g) of the sensor through the responsivity, so it can be seen that NETD is independent of the gain if there is no limitation imposed by the limited capacity of the ROIC capacitors. When the FPA is exposed to substantial

photon flux, the integration time should be adjusted to prevent the ROIC capacitors from saturating (read-out limited case). On the contrary, when the FPA is under low background or high frame rate (low integration time) conditions, large gain is needed to fill the ROIC capacitors. In this sense, ROIC noise is significant in determining the system sensitivity. NETD of the FPA can be expressed under this condition as [12]

$$NETD = \frac{kT^2 Q_{ROIC}}{\varphi_B q\eta g\tau} \quad (3.8)$$

where Q_{ROIC} is the noise charge of the ROIC, and φ_B is the background radiation power. It can be seen that NETD becomes inversely proportional to the gain and integration time. If the integration time is limited by the application (high frame rate), large gain is required for a small NETD values.

The noise- and photo-electrons generated by a fully BLIP QWIP FPA pixel with dimensions of $20 \times 20 \mu\text{m}^2$ were calculated [50]. Figure 3.2 shows the results while the detector is looking at 240 and 290 K with $f/2$ optics, different integration times and two different gain values (0.3 and 1). It is assumed that the detector is sensitive in a range of 8.0-9.0 μm with peak $\eta=10\%$. The calculations are made for different gain values ($g=0.3$ is typical for AlGaAs/GaAs QWIPs). The noise (800 e^-) and 50% electron capacity ($5 \times 10^6 e^-$) levels of a typical ROIC are also shown in the figure for comparison.

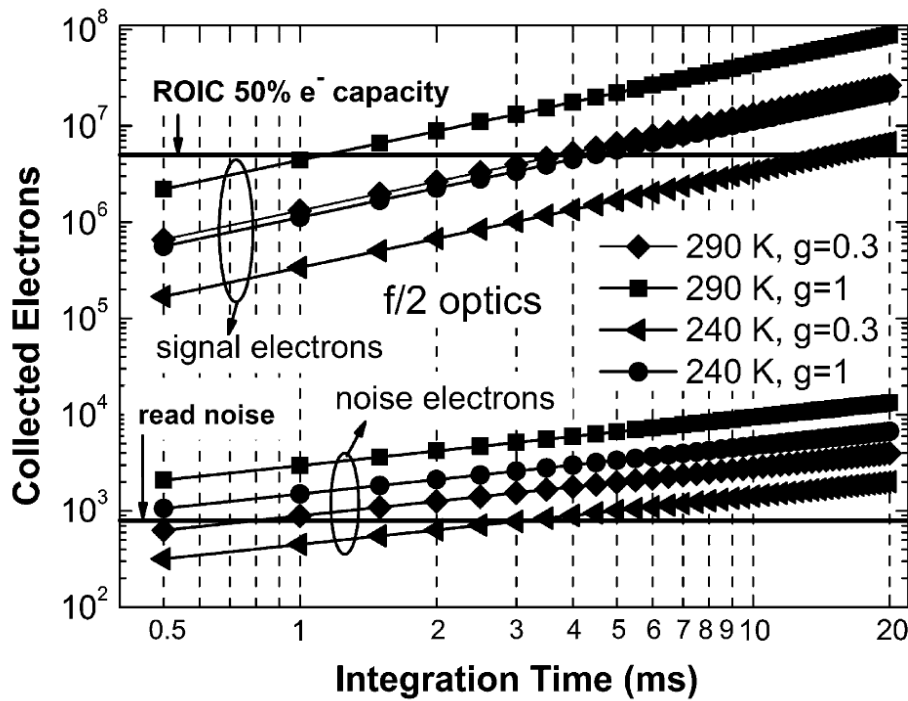


Figure 3.2: Noise- and photo-electrons generated by a $20 \times 20 \mu\text{m}^2$ FPA pixel operating in the wavelength range $8.0\text{-}9.0 \mu\text{m}$ looking at 240 and 290 K blackbody targets with $f/2$ aperture [50].

According to the results, the sensitivity of the imaging system is limited by the ROIC noise under low background/short integration time conditions when the device gain is low ($g \sim 0.3$). This low level of gain is observed in a typical AlGaAs/GaAs QWIP. In case the integration time is limited at 1.5 ms by the application, in order to fill half of a typical ROIC capacitor the detector needs to have large gain ($g=1$) while looking at 290 K with $f/2$ aperture. While looking at 240 K target, the integration time must be larger than 10 ms and 4 ms with the detector gain levels of 0.3 and 1, respectively.

Figure 3.3 shows the characteristic of a desirable QWIP with flexible behavior [50]. In the case of sufficiently high photon flux and integration time, the gain of the device should be adjusted to low values. On the other hand, it should be arranged to large values under low photon flux and/or low integration time.

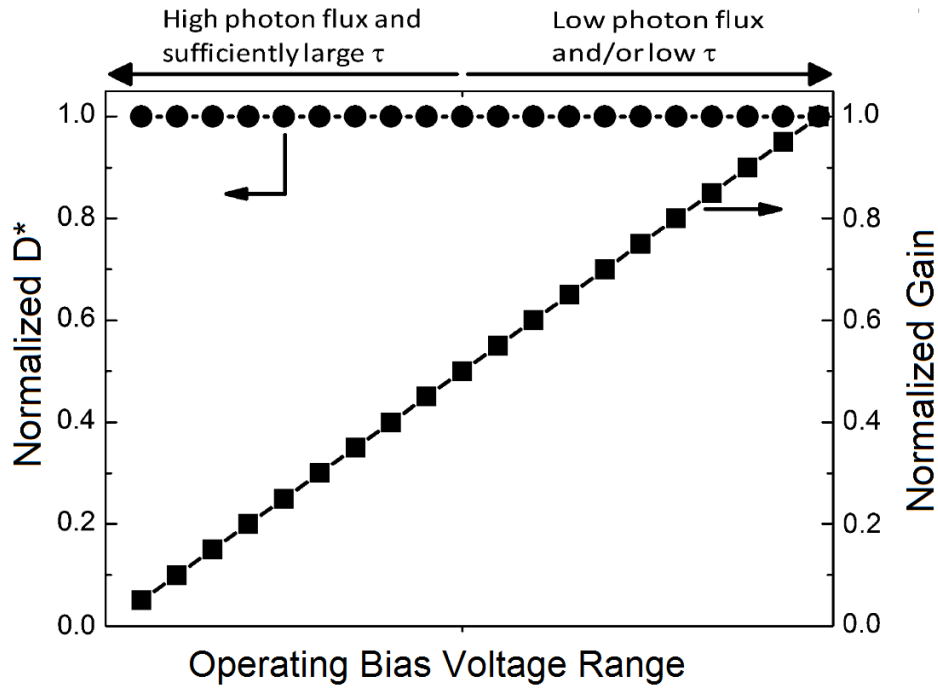


Figure 3.3: Gain and sensitivity of a desirable QWIP [50]

3.2 QWIP Design on InP Substrate

There are several parameters that must be considered for optimum design of the QWIP structure. These parameters must be optimized according to the desired application, the desired peak and cut-off wavelength, the desired sensitivity, the desired operating temperature, and environmental conditions.

Firstly, the well width and the potential barrier height should be determined for the desired peak and cut-off wavelength. Indium mole fraction in InGaAs well material determines the barrier height. For the operating wavelength both In mole fraction and well width need to be considered.

The dependency of the peak wavelength on the well width and In mole fraction(x) in B-B and B-C InP/ $\text{In}_x\text{Ga}_{1-x}\text{As}$ structures is given in the study of Gusakov et al.

[40]. InP/ $\text{In}_x\text{Ga}_{1-x}\text{As}$ QWIP is lattice matched when $x=0.53$ and in this case peak responsivity wavelength is around $8\ \mu\text{m}$ which is short for LWIR detection.

A slight change in the well width can not be enough to adjust the wavelength because ground state changes with first excited state of quantum well almost at the same amount. Thus, the value of x should be altered in order to lengthen the operating wavelength beyond $8\ \mu\text{m}$. However, it should be kept as close to 0.53 as possible in order not to increase strain too much. As a result, $x=0.48$ and the well width of $50\text{-}60\ \text{\AA}$ is suitable for LWIR detection according to theoretical results [40].

Another important parameter is the quantum well doping density which directly affects the detector performance. The absorption quantum efficiency increases linearly with the doping density [51], while the dark current increases exponentially [21]. For optimum BLIP temperature and maximum detectivity the doping density needs to be optimized.

The barrier width also plays an important role for the dark current of QWIP. The barrier should be chosen wide enough in order to minimize the dark current arising from the ground state sequential tunneling and should be thin enough not to increase the total layer thickness unnecessarily. In order to minimize the dark current and optimize the period length, the optimized barrier width can be around $400\ \text{\AA}$.

Period number (N) is another parameter that affects the device performance. Even though the period number does not affect the detector responsivity, it provides larger quantum efficiency when it is increased. However, when N is increased, a larger bias voltage should be applied to obtain the same responsivity, and the bias voltage applicable by a read out integrated circuit is limited.

3.3 InP/InGaAs LWIR QWIPs

3.3.1 QWIP Epilayer Structure

In order to investigate the feasibility of InP based LWIR QWIPs, an InP/InGaAs LWIR QWIP structure is fabricated and characterized through collaboration with Y. Arslan in this study. We had the InP/InGaAs epilayer structure shown in Figure 3.4 grown on 3-inch semi-insulating InP substrate by solid source molecular beam epitaxy. The structure is strained with an In mole fraction of 0.48. The purpose of using the strained quantum well structure is to lengthen the cut-off wavelength beyond 8.5 μm .

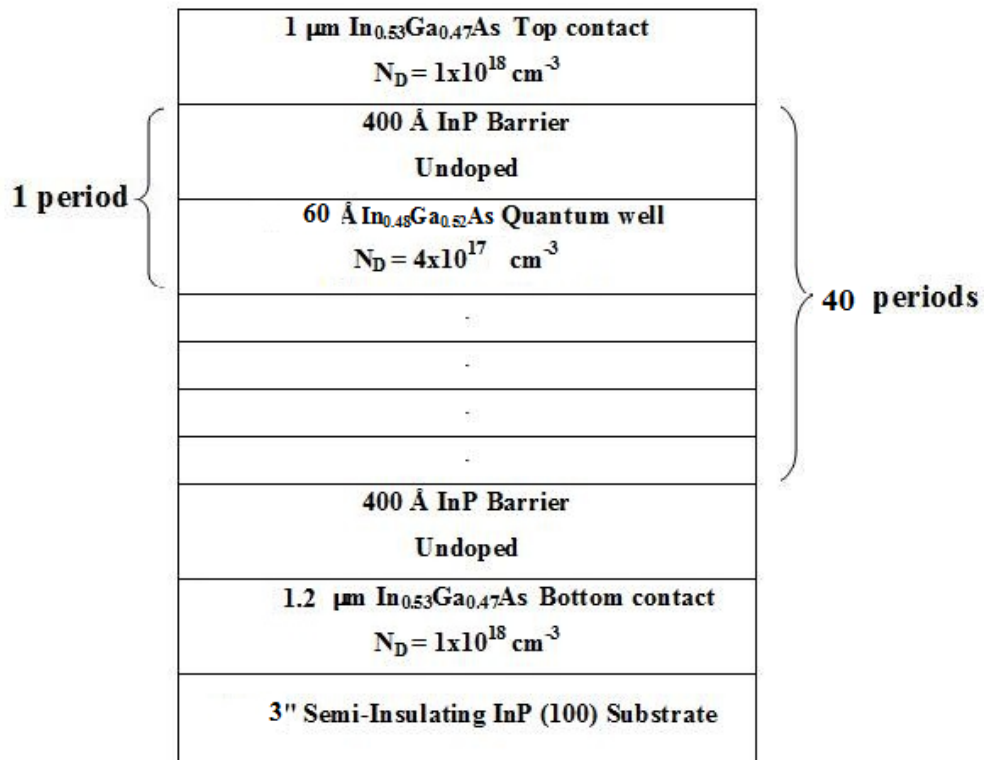


Figure 3.4: Epilayer structure of the InP/InGaAs QWIP

The QWIP epilayer structure consists of forty 60 Å thick $\text{In}_{0.48}\text{Ga}_{0.52}\text{As}$ quantum wells (QWs) which were sandwiched between 400 Å thick undoped InP barriers. The top and bottom $\text{In}_{0.53}\text{Ga}_{0.47}\text{As}$ contacts layers are n-type doped at $N_D=1 \times 10^{18} \text{ cm}^{-3}$ and 1 and 1.2 μm thick, respectively. QWs are n-type doped at $N_D=4 \times 10^{17} \text{ cm}^{-3}$ (with the density of 2D electrons in the QW (n_{2D}) of $2.4 \times 10^{11} \text{ cm}^{-2}$).

3.3.2 InP/InGaAs QWIP FPA on InP Substrate

A large format (640x512) InP/InGaAs QWIP array was fabricated through the steps given in section 2.3 by using the above epilayer structure. The formation of the optical grating structure by dry etching was the first step of the fabrication. Then 25 μm pitch mesas were formed by optical lithography and reactive ion etching (RIE) using an inductively coupled plasma system. After the deposition of the ohmic contacts, reflector and passivation layer, under bump metallization was performed and indium bumps were uniformly formed by e-beam evaporation process. The array was hybridized to Indigo ISC9803 ROIC by a flip-chip aligner/bonder and underfill injection was performed. Finally the substrate was thinned to ~10 μm.

InP/InGaAs test detectors were fabricated through the above FPA process together with the FPA pixels. Test detectors were used for the pixel level characterization since they had all the features of the FPA pixels. For pixel level electrical and optical characterization, the test detectors were flip-chip bonded to a fan-out substrate and parallel connected for reliable electrical and optical measurements due to their high electrical resistances.

After the test detector fabrication, detailed experimental characterization was performed by mounting the detector to a liquid nitrogen cooled test dewar. Responsivity spectrum of the test detectors were measured with a Fourier-Transform Infrared Spectrometer (FTIR). First of all, the emission spectrum of the blackbody source of the FTIR spectrometer was measured with a reference detector whose response is wavelength independent. Then the fabricated test detectors were

placed in the FTIR system and the responsivity spectra were measured under various reverse bias voltages (mesa top negative). Later, the measured data was divided with the reference data by the FTIR software. The characteristics of the blackbody source and the absorption of air were cancelled by this way. Figure 3.5 shows the test setup schematically.

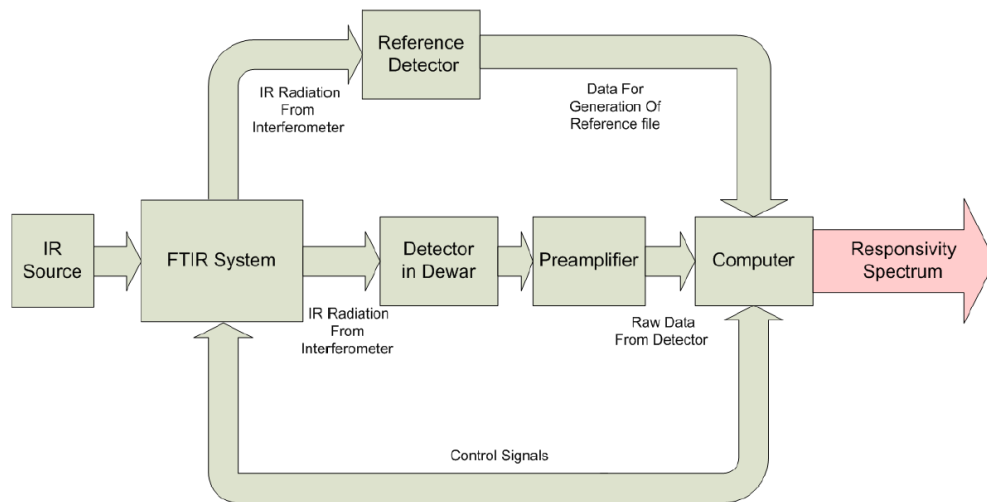


Figure 3.5: The responsivity spectrum measurement setup [52]

The normalized responsivity spectra of the fabricated QWIP test detectors were determined at operating temperature of 67 K as shown in Figure 3.6. QWIP responsivity peaks at 8.5 μm wavelength with $\sim 9 \mu\text{m}$ cut-off wavelength and $\Delta\lambda/\lambda_p$ of 15%. The characteristics of the fabricated InP/InGaAs QWIPs were compared with those of an AlGaAs/GaAs QWIP with a similar spectral responsivity as shown in Fig. 3.6.

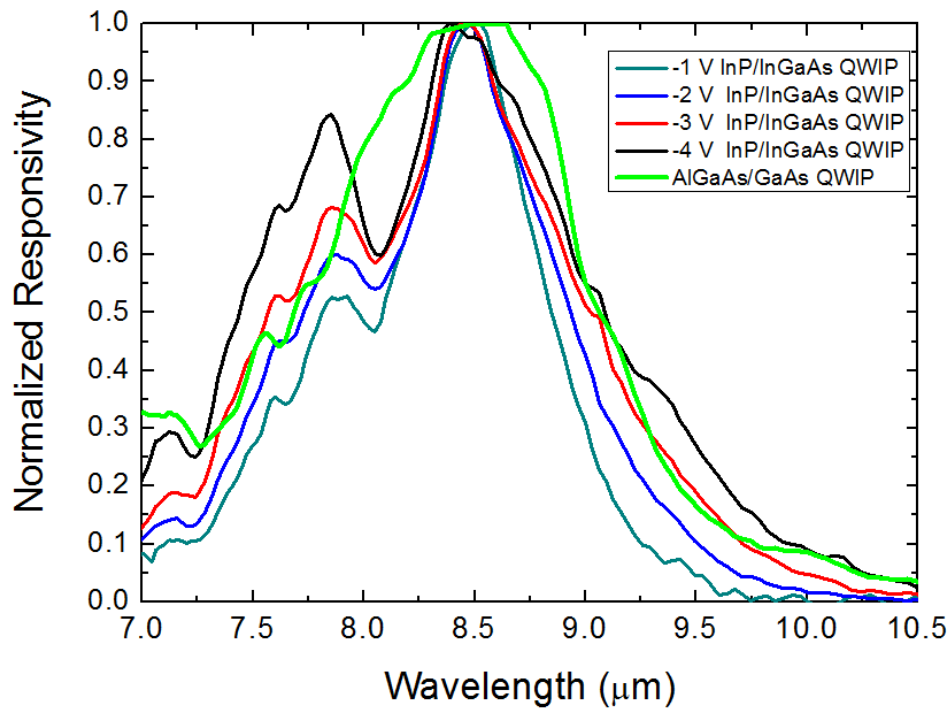


Figure 3.6: Responsivity spectrum of the QWIP test structures

Current-voltage (I-V) measurements of the fabricated test detectors were conducted at different temperatures with Keithley Model 236 source-measure unit under dark and illuminated conditions. The measured dark current versus bias characteristics of a single FPA pixel ($20 \times 20 \mu\text{m}^2$) at 67 K and the photocurrent with f/1.5 optics (300 K background) are given in Figure 3.7. The detector shows BLIP characteristic up to 4.5 V reverse bias at 67 K with f/1.5 optics.

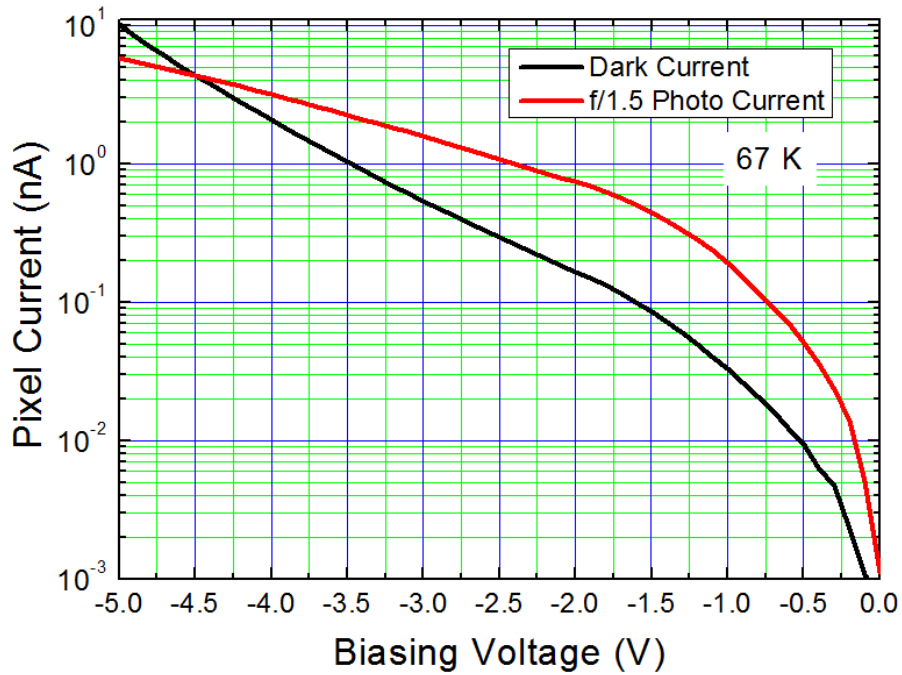


Figure 3.7: Dark current and photocurrent characteristics of QWIP test structures

Figure 3.8 shows the I-V characteristics of the InP/In_{0.48}Ga_{0.52}As QWIP in comparison with that of the AlGaAs/GaAs QWIP. Although the AlGaAs/GaAs QWIP provides smaller dark current than InP/InGaAs QWIP under moderate and large reverse biases, it displays larger dark current under positive bias. InP/InGaAs QWIP provides smaller dark current under positive bias similar to the results reported by Gunapala et al. [53]. This result can be explained by a lower barrier in InGaAs on InP interface than that in the InP on InGaAs interface reflecting an asymmetry.

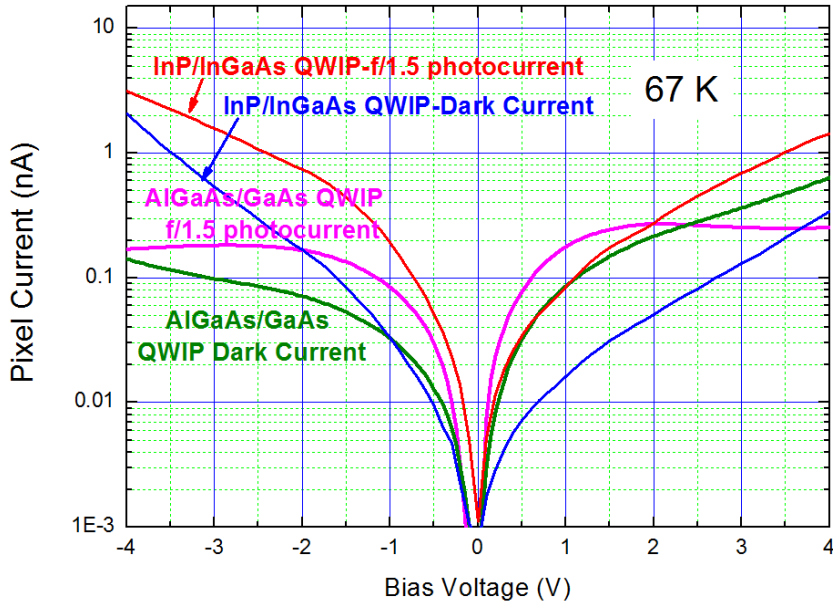


Figure 3.8: I-V characteristics of InP/InGaAs QWIP in comparison with the AlGaAs/GaAs QWIP

Responsivity and detectivity measurement setup illustrated in Figure 3.9 consists of a blackbody source, a chopper, a current preamplifier, lock-in amplifier and a PC with specialized software. Detector was placed at a measured distance from the blackbody source whose radiation was modulated with the chopper. The detector was connected to the preamplifier which biases the detector. The lock-in amplifier measures the detector response to the blackbody by correlating the chopper frequency and the measured lock-in amplifier frequency. The measured detector signal was divided by the optical power falling on the detector by the software and the blackbody voltage responsivity was obtained. The blackbody current responsivity could be calculated by multiplying the voltage responsivity with the gain of the preamplifier.

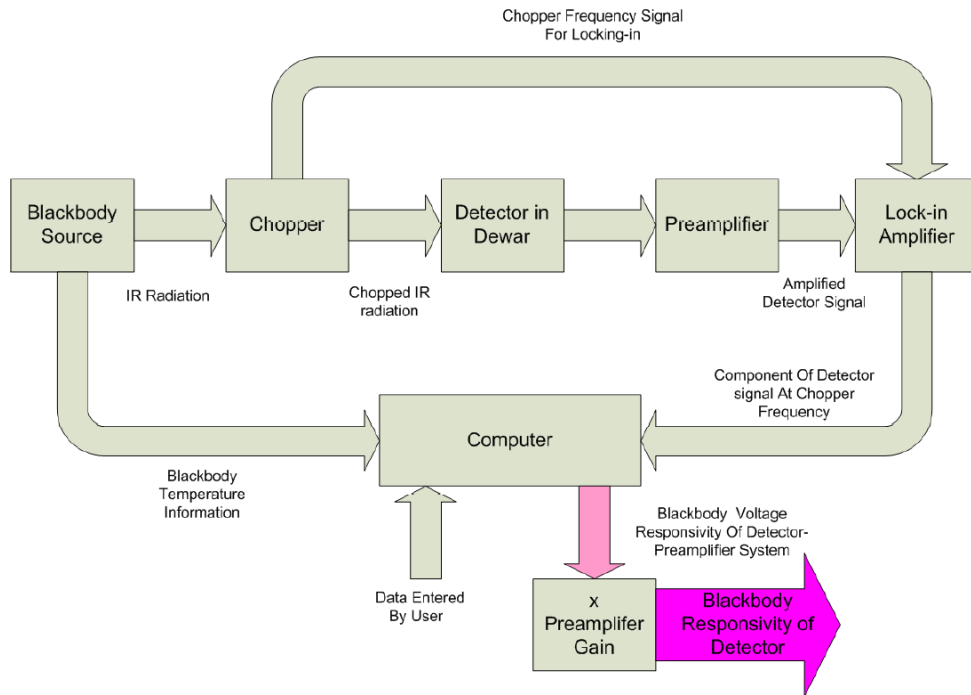


Figure 3.9: Responsivity and detectivity measurement setup [52]

In the blackbody responsivity measurements, the measured detector power is assumed as total emitted power by the blackbody source. In order to determine the peak responsivity, the shape of the responsivity spectrum of the detector must be considered. Peak factor was calculated by dividing the integrated blackbody spectrum by the detector spectrum. The peak factor calculation is shown in Figure 3.10. As a result, the peak responsivity values were calculated by multiplying the blackbody responsivity values with the peak factor. Figure 3.11 shows the calculated peak responsivity values of the test detector.

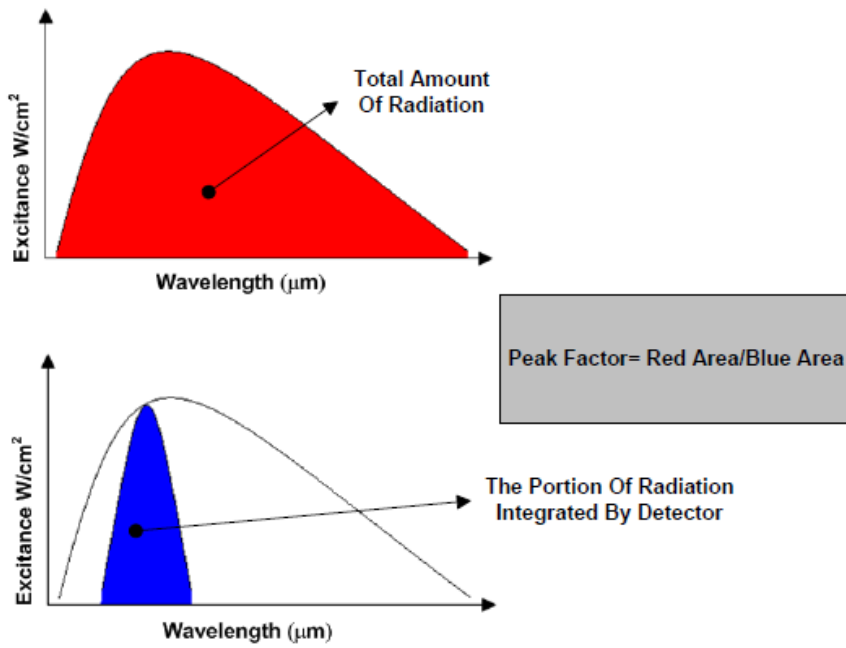


Figure 3.10: Peak factor calculation procedure [52]

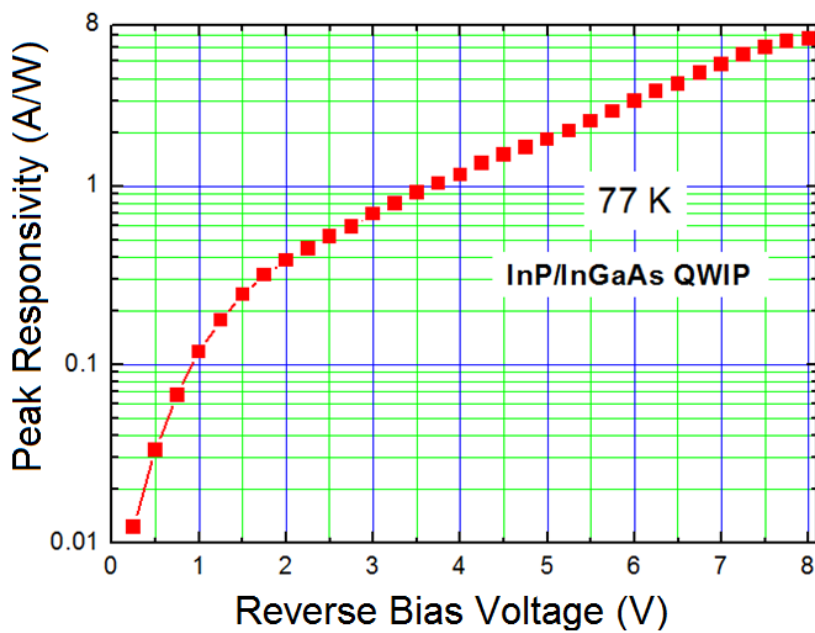


Figure 3.11: Peak responsivity values of the InP/InGaAs QWIP test structure

After the responsivity measurements, detector noise was measured when the detector was looking at 300 K background. The measurements were conducted with a low noise preamplifier and lock in amplifier at 1527 Hz at 77 K operating temperature. Once the noise level is measured, the noise gain can be calculated at different applied bias voltages according to the following equation:

$$g_n = \frac{i_n^2}{4qI\Delta f} \quad (3.9)$$

The noise gain of the detector is expected to be nearly equal to the photoconductive gain under moderately large bias voltages. In that case peak quantum efficiency of the device is determined to be 20% being larger than that of AlGaAs/GaAs QWIP by nearly a factor of five. The photoconductive (g_p) and noise (g_n) gain values versus bias voltage are shown in Figure 3.12. The noise gain deviates from the photoconductive gain under large bias voltages which is attributed to impact ionization [54]. Since the the obtained characteristics suggest the presence of other noise mechanisms (in addition to G-R noise), g_n (extracted from the G-R noise expression) under moderate and large bias voltages is shown only for illustrative purposes in Fig. 3.12.

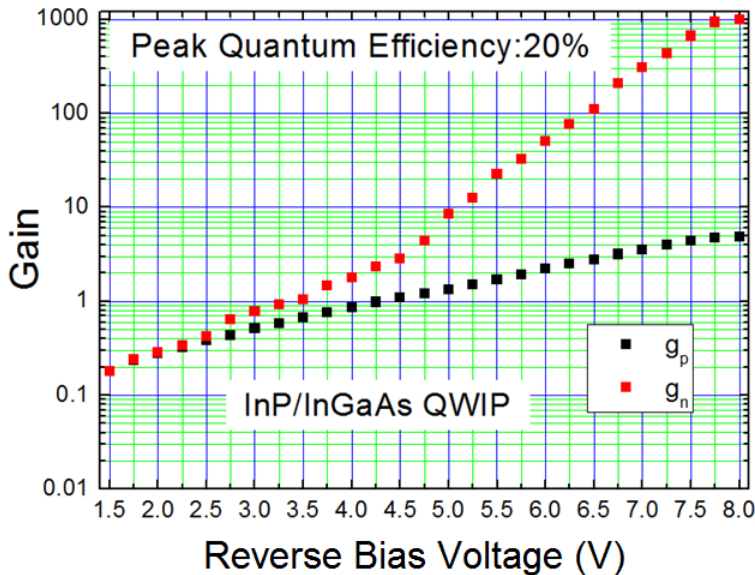
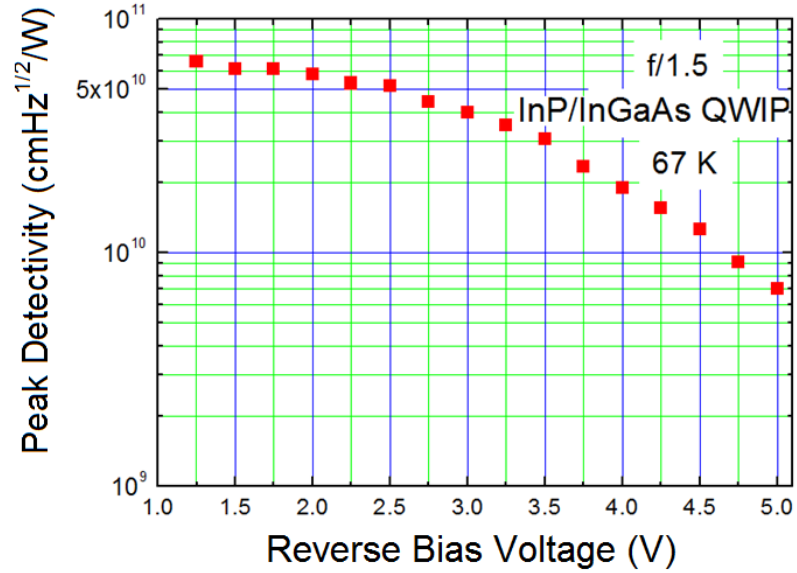
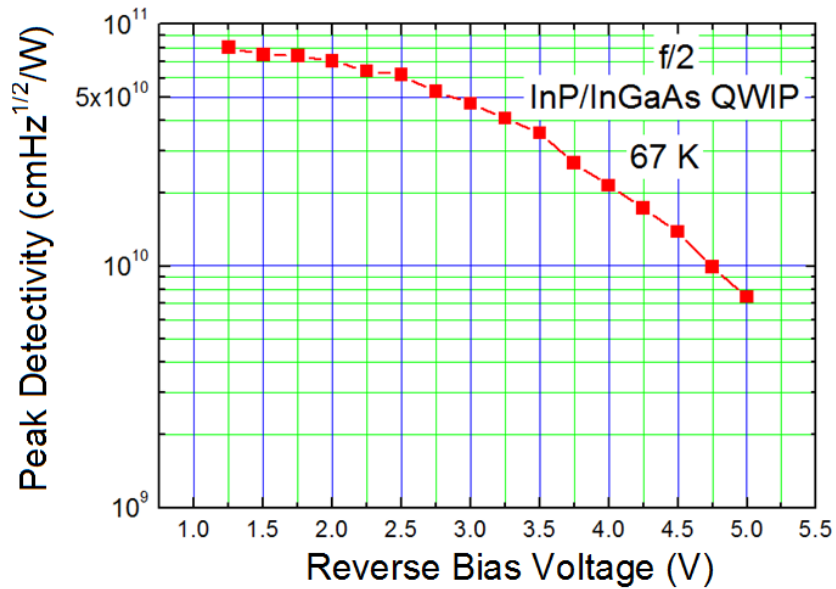


Figure 3.12: Noise gain and photoconductive gain values

Figure 3.13 shows the peak detectivity values of the detector with two different f-numbers optics.



a)



b)

Figure 3.13: Peak detectivity of the test detectors with a) f/1.5 aperture, b) f/2 aperture

As a result of the peak responsivity and detectivity measurements, it can be said that InP/InGaAs QWIPs provide reasonably high detectivities with impressively large responsivities. The conversion efficiency of the InP/InGaAs QWIP ($\eta.g=17\%$ under 4 V) is significantly larger than that of AlGaAs/GaAs QWIP ($\eta.g=1.2\%$ under 4 V). Figure 3.14 shows the peak responsivity and noise gain of the AlGaAs/GaAs QWIP which was fabricated and characterized by a colleague. Conversion efficiency versus reverse bias voltage plot of the InP based QWIP is shown in Figure 3.15. Conversion efficiency of InP based QWIP is larger than the GaAs based QWIP since the InP/InGaAs QWIP provides both higher gain and larger quantum efficiency. It should also be noted that the above results should not be used for direct quantitative comparison of InP/InGaAs and AlGaAs/GaAs QWIPs due to n_{2D} difference in the quantum wells of these devices and processing differences. However, the larger gain and quantum efficiency in InP/InGaAs QWIPs is obvious.

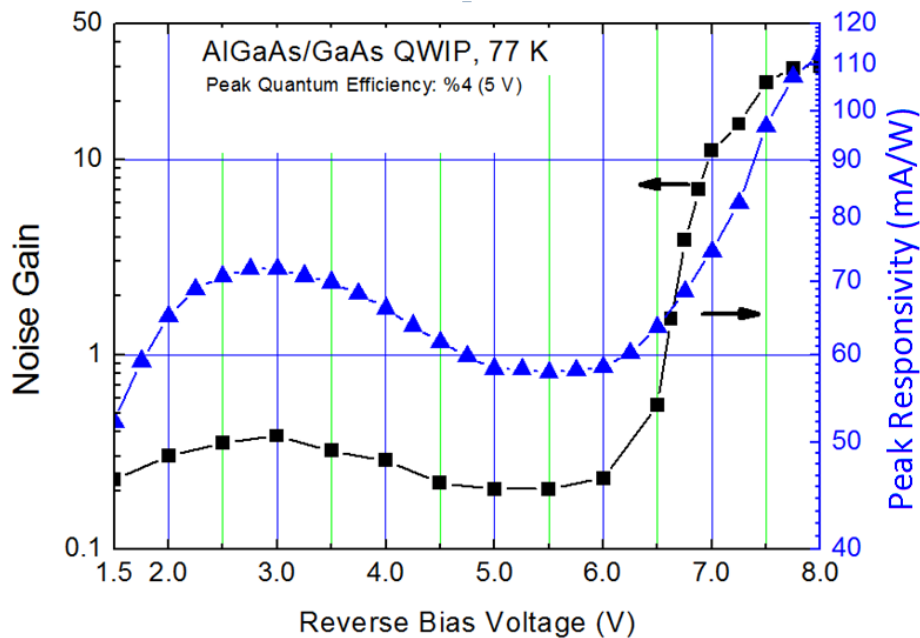


Figure 3.14: The peak responsivity and noise gain of the AlGaAs/GaAs QWIP

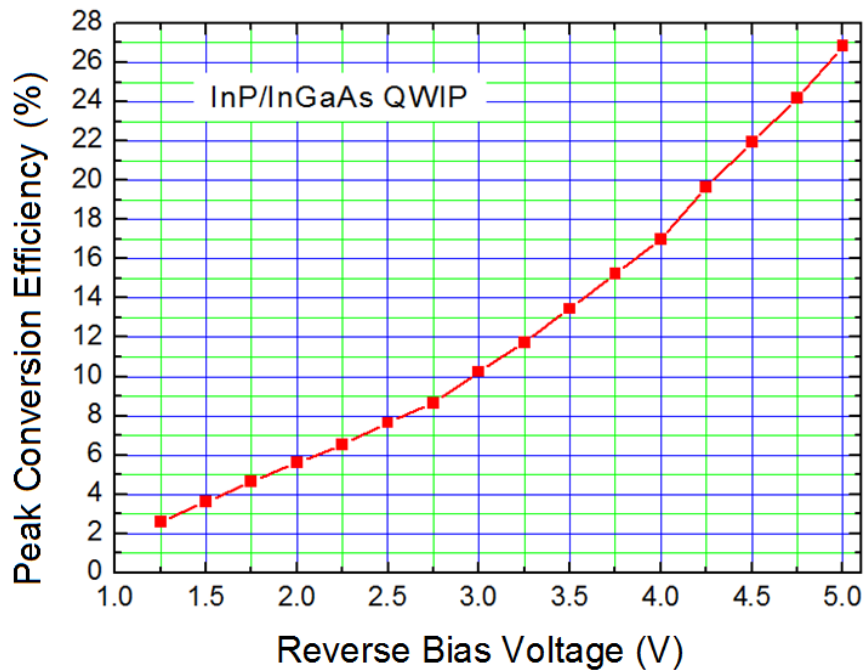


Figure 3.15: Conversion efficiency of InP/InGaAs QWIP

While the detectivity is kept at a sufficiently high level, the gain of the InP/InGaAs QWIP can be varied in a wide range with the applied bias. The photoconductive gain changes by nearly an order of magnitude when the bias voltage is changed in the range of 1.5-4 V. Therefore, InP/InGaAs QWIP has a variable gain flexibility as a desirable QWIP characteristic as explained in section 3.1. However, this situation is not achievable for AlGaAs/GaAs QWIPs due to the saturation of the gain (drift distance) at considerably smaller values (~ 0.3) [21].

Following the single pixel characterization, FPA level characterization was conducted by the members of our research group. The fabricated FPA was located in a dewar with f/1.5 optics at 68 K detector temperature. Without field of view correction and any calibration, the DC signal and NETD nonuniformities of the FPA are as low as 6% and 18% at 68 K detector temperature, respectively. Fig 3.16 shows the measured NETD of the FPA with half filled read-out circuit capacitors.

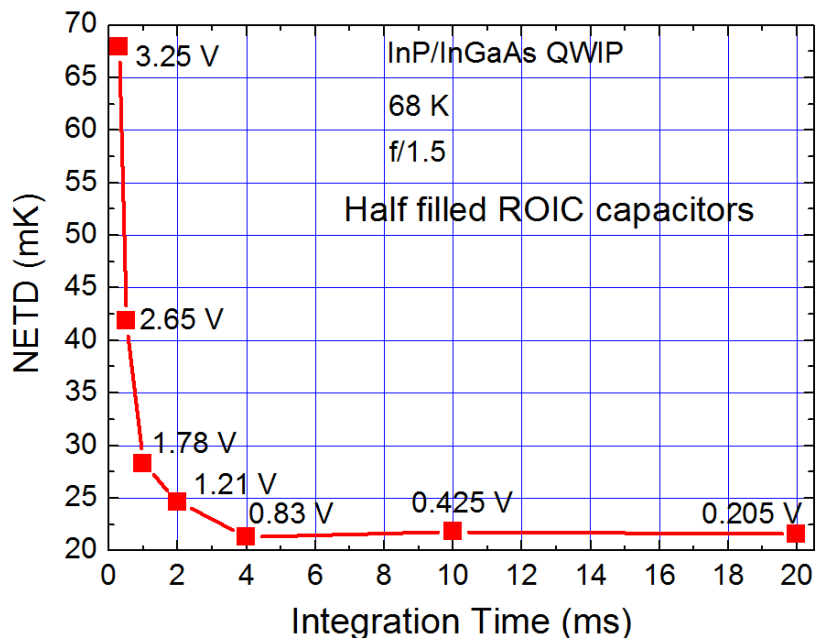


Figure 3.16: Measured NETD values at 68 K

NETD of the FPA is as low as 25 mK with an integration time as short as 2 ms, $f/1.5$ aperture and 1.21 V bias voltage at 68 K detector temperature. The operability of the FPA is 99.7% .

Figure 3.17 shows a thermal image recorded with this FPA at an operation temperature of 68 K and integration time of 3 ms with $f/2$ optics



Figure 3.17: A thermal image recorded with the InP/InGaAs FPA at an operation temperature of 68 K and integration time of 3 ms with f/2 optics

3.4 Conclusion

In this chapter, advantages of the strained InP/InGaAs material system for LWIR QWIPs over the standard AlGaAs/GaAs QWIPs are discussed. A large format strained InP/In_{0.48}Ga_{0.52}As QWIP FPA with a cut-off wavelength of 9 μm is investigated. The detailed pixel level and FPA level characterization were conducted. The test detectors which are identical to FPA pixels provided desirable characteristics with an impressively high quantum efficiency and large responsivity in the bias region where the detectivity is reasonably high. The InP based QWIP FPA offers relatively high gain which increases the design flexibility.

The requirements of most low integration time/low background applications are satisfied by the InP/InGaAs QWIP FPA. On the other hand, AlGaAs/GaAs QWIPs may not be suitable for such applications because of low conversion efficiency.

CHAPTER 4

CONCLUSION

In this thesis work, a large format (640x512) InP/InGaAs QWIP FPA is fabricated and characterized. The comparison between the InP based QWIPs and standard GaAs based QWIPs is performed and the advantages of the InP based QWIPs over the GaAs based QWIPs are presented. AlGaAs/GaAs QWIPs used for LWIR band imaging suffer from low conversion efficiency under high frame rate and/or low background conditions. In order to improve the imaging capability of QWIP technology alternative material systems should be utilized. In this work, an InP/InGaAs LWIR QWIP has been demonstrated in order to show the high potential of this material system for overcoming the bottlenecks of the standard QWIP material system.

The conclusion of this thesis encourages the usage of the InP/InGaAs material system for LWIR QWIP applications. The slightly strained InP/In_{0.48}Ga_{0.52}As QWIP FPA provides excellent characteristics with an impressively high peak quantum efficiency of 20% and a broad spectral response ($\Delta\lambda/\lambda_p=15\%$). In addition to this, the FPA has a wide range of gain values offering an additional design flexibility of thermal imagers. High conversion efficiency with a sufficiently high detectivity is a requirement for applications such as tracking of rapidly moving targets due to the need for low integration times. The FPA satisfies the requirements of most low integration time/low background applications where AlGaAs/GaAs QWIPs suffer from low conversion efficiency [41].

To sum up, InP/InGaAs material system as an alternative to AlGaAs/GaAs provides high potential for LWIR band QWIP FPAs by providing high conversion efficiency under high frame rate (low integration time) and/or low background conditions.

As a further work, the optimization of the epilayer structure of the InP/InGaAs QWIPs may be conducted in order to maximize the detectivity or the BLIP temperature. Such a study should involve the growth, fabrication and characterization of InP/InGaAs QWIPs with various quantum well doping densities at the targeted peak and cut off wavelengths which are set by the quantum well width and the In mole fraction in InGaAs.

REFERENCES

- [1] F. Systems, "ThermoVision SC4000-SC6000 User's Guide," July 2007. [Online]. Available: <http://digitalcorpora.org/corp/nps/files/govdocs1/132/132872.pdf>. [Accessed November 2011].
- [2] A. Rogalski, J. Antoszewski and L. Faraone, "Third-Generation Infrared Photodetector Arrays," *Journal of Applied Physics*, vol. 105, pp. (091101)1-44, 2009.
- [3] E. Barr, "The Infrared Pioneers-III. Samuel Pierpont Langley," *Infrared Physics*, vol. 3, pp. 195-206, 1963.
- [4] T. Case, "Notes on the Change of Resistance of Certain Substances in Light," *Physical Review*, vol. 9, no. 4, pp. 305-310, 1917.
- [5] R. Cushman, "Film-type Infrared Photoconductors," *Proceedings of IRE*, vol. 47, pp. 1471-1475, 1959.
- [6] S. Uc Sharma, "Infrared Detectors," Electronic Systems Group, EE Dept, Bombay, M. Tech Credit Seminar Report, 2004.
- [7] A. Rogalski, *Infrared Detectors*, CRC Press, 2011.
- [8] C. Beşikci, Lecture notes on Infrared Device and Systems, Lecture notes, 2008.
- [9] S. Ozer, "InSb and InAsSb Infrared Photodiodes on Alternative Substrates and InP/InGaAs Quantum Well Infrared Photodetectors : Pixel And Focal Plane Array Performance," PhD. Thesis, METU, 2005.
- [10] A. Rogalski and K. Chrzanowski, "Infrared Devices and Techniques," *Opto-electronics Review*, vol. 10, no. 2, pp. 111-136, 2002.
- [11] S. Eker, "Single and Dual-Band Quantum Well Infrared Photodetector Focal Plane Arrays on InP Substrates," PhD. Thesis, METU, 2010.
- [12] H. Schneider and H. Liu, *Quantum Well Infrared Photodetectors: Physics and Applications*, Springer Series in Optical Sciences, 2007.
- [13] J.D.Vincent, *Fundamentals of Infrared Detector Operation and Testing*, Wiley, 1990.
- [14] A. Daniels, *Field Guide to Infrared Systems*, SPIE Press, 2007.
- [15] S. Gunapala and S. Bandara, "Quantum Well Infrared Photodetector (QWIP) Focal Plane Arrays," *Semiconductors and Semimetals*, vol. 62, pp. 1-83, 1999.

- [16] L. Esaki and R. Tsu, "Superlattice and Negative Differential Conductivity in Semiconductors," *IBM Journal of Research and Development*, pp. 62-65, 1970.
- [17] B. Levine, K. Choi, C. Bethea, J. Walker and R. Malik, "New 10 μm Infrared Detector Using Intersubband Absorption in Resonant Tunneling GaAlAs Superlattices," *Applied Physics Letters*, vol. 50, no. 16, pp. 1092-1094, 1987.
- [18] O.O.Cellek, "Ensemble Monte Carlo Simulation of Quantum Well Infrared Photodetectors, and InP Based LWIR QWIPs for Thermal Imaging," PhD. Thesis, METU, 2006.
- [19] K. Choi, D. Forrai, D. Endres, J. Sun, P. Pinsukanjana and J. Devitt, "C-QWIP Focal Plane Arrays," *Infrared Physics and Technology*, vol.52, pp. 364-370, 2009.
- [20] M. Z. Tidrow, "QWIP and MCT for Long Wavelength and Multicolor Focal Plane Applications," Army Research Laboratory, Washington, 1998.
- [21] B. Levine, "Quantum Well Infrared Photodetectors," *Journal of Applied Physics*, vol. 74, no. 8, pp. R1-R81, 1993.
- [22] K. Choi, S. Bandara, S. Gunapala, W. Liu and J. Fastenau, "Detection Wavelength of InGaAs/AlGaAs Quantum Wells and Superlattices," *Journal of Applied Physics*, vol. 91, no. 2, pp. 551-564, 2002.
- [23] O. Cellek, S. Ozer and C. Beşikci, "High Responsivity InP/InGaAs Quantum Well Infrared Photodetectors: Characteristics and Focal Plane Array Performance," *IEEE Journal of Quantum Electronics*, vol. 41, pp. 980-985, 2005.
- [24] O. Cellek and C. Beşikci, "Detailed Investigation of Electron Transport, Capture and Gain in $\text{Al}_{0.3}\text{Ga}_{0.7}\text{As}/\text{GaAs}$ Quantum Well Infrared Photodetectors," *Semiconductor Science and Technology*, vol. 19, pp. 183-190, 2004.
- [25] A. Cho, "Film Deposition by Molecular Beam Techniques," *Journal of Vacuum Science and Technology*, vol. 8, pp. S31-S38, 1971.
- [26] [Online]. Available: http://projects.ece.utexas.edu/ece/mrc/groups/street_mbe/mbechapter.html. [Accessed 7 2012].
- [27] A. Rogalski, "Infrared Detectors: Status and Trends," *Progress in Quantum Electronics*, vol. 27, no. 2-3, pp. 59-210, 2003.
- [28] S. Gunapala, S. Bandara, J. Liu, C. Hill, S. Rafol, J. Mumolo, J. Trinh, M. Tidrow and P. LeVan, "1024x1024 Pixel Mid-Wavelength and Long-Wavelength Infrared QWIP Focal Plane Arrays for Imaging Applications," *Semiconductor Science and Technology*, vol. 20, pp. 473-480, 2005.
- [29] M. Sundaram, S. Wang, M. Taylor, A. Reisinger, G. Milne, K. Reiff, R. Rose and R. Martin, "Two-Color Quantum Well Infrared Photodetector Focal Plane Arrays," *Infrared Physics and*

Technology, vol. 42, pp. 301-308, 2001.

- [30] S. Bandara, S. Gunapala, J. Liu, S. Rafol, D. Ting, J. Mumolo, R. Chuang, T. Trinh, J. Liu, K. Choi, M. Jhabvala, J. Fastenau and W. Liu, "Four-Band Quantum Well Infrared Photodetector Array," *Infrared Physics and Technology*, vol. 44, pp. 369-375, 2003.
- [31] S. Gunapala, S. Bandara, J. Liu, J. Mumolo, D. Ting, C. Hill, J. Nguyen, B. Simolon, J. Woolaway, S. Wang, W. Li, P. LeVan and M. Tidrow, "1024x1024 Format Pixel Co-located Simultaneously Readable Dual-Band QWIP Focal Plane," *Infrared Physics and Technology*, vol. 52, pp. 395-398, 2009.
- [32] K. Choi, M. Jhabvala and R. Peralta, "Voltage-Tunable Two-Color Corrugated-QWIP Focal Plane Arrays," *IEEE Electron Device Letters*, vol.29, pp. 1011-1013, 2008.
- [33] Y. Arslan, S. Eker, M. Kaldirim and C. Besikci, "Large Format Voltage Tunable Dual-Band QWIP FPAs," *Infrared Physics and Technology*, vol.52, p. 399-402, 2009.
- [34] S. Gunapala, B.F. Levine, D. Ritter, R. Hamm and M. Panish, "InGaAs/InP Long Wavelength Quantum Well Infrared Photodetectors," *Applied Physics Letters*, vol. 58, pp. 2024-2026, 1991.
- [35] J. Andersson, L. Lundqvist, Z. Paska, K. Streubel and J. Wallin, "Long-Wavelength Quantum-Well Infrared Detectors Based on Intersubband Transitions in InGaAs/InP Quantum Wells," *Proceedings of SPIE*, vol. 162, pp. 216-226, 1992.
- [36] C. Jelen, S. Slivken, T. David, M. Razeghi and G. Brown, "Noise Performance of InGaAs-InP Quantum-Well Infrared Photodetectors," *IEEE Journal of Quantum Electronics*, vol. 34, pp. 1124-1128, 1998.
- [37] D. Sengupta, S. Jackson, A. Curtis, W. Fang, J. Malin, T. Horton, Q. Hartman, H. Kuo, S. Thomas, J. Miller, K. Hsieh, I. Adesida, S. Chuang, M. Feng, G. Stillman, Y. Chang, W. Wu, J. Tucker, H. Chen, J. Gibson, J. Mazumder, L. Li and H. Liu, "Growth and Characterization of n-Type InP/InGaAs Quantum Well Infrared Photodetectors for Response at 8.93 μm ," *Journal of Electronic Materials*, vol. 26, pp. 1376-1381, 1997.
- [38] A. Majumdar, A. Shah, M. Gokhale, S. Sen, S. Ghosh, B. Arora and D. Tsui, "High-Responsivity High-Gain $\text{In}_{0.53}\text{Ga}_{0.47}\text{As}$ -InP Quantum-Well Infrared Photodetectors Grown Using Metal-Organic Vapor Phase Epitaxy," *IEEE Journal of Quantum Electronics*, vol. 41, pp. 872-878, 2005.
- [39] S. Ozer, U. Tumkaya, B. Asici and C. Besikci, "Demonstration and Performance Assessment of Large Format InP-InGaAsP Quantum Well Infrared Photodetector Focal Plane Array," *IEEE Journal of Quantum Electronics*, vol. 43, pp. 709-713, 2007.
- [40] Y. Gusakov, E. Finkman, G. Bahir and D. Ritter, "The Effect of Strain in InP/InGaAs Quantum-Well Infrared Photodetectors on the Operating Wavelength," *Applied Physics Letters*, vol. 79, pp. 2508-2510, 2001.

- [41] S. Eker, Y. Arslan, A. Onuk and C. Besikci, "High Conversion Efficiency InP/InGaAs Quantum Well Infrared Photodetector Focal Plane Array with 9.7 μm Cut-Off for High Speed Thermal Imaging," *IEEE Journal of Quantum Electronics*, vol.46, pp. 164-168, 2010.
- [42] S. Gunapala, B. Levine, D. Ritter, R. Hamm and M. Panish, "Lattice Matched InGaAsP/InP Long-Wavelength Quantum-Well Infrared Photodetectors," *Applied Physics Letters*, vol. 60, pp. 636-638, 1992.
- [43] B. Levine, A. Cho, J. Walker, R. Malik, D. Kleinmen and D. Sivco, "InGaAs/InAlAs Multiquantum Well Intersubband Absorption at a Wavelength of $\lambda=4.4 \mu\text{m}$," *Applied Physics Letters*, vol. 52, pp. 1481-1483, 1988.
- [44] G. Hasnain, B. Levine, D. Sivco and A. Cho, "Mid-infrared Detectors in the 3-5 μm Band Using Bound to Continuum State Absorption in InGaAs/InAlAs Multi-Quantum Well Structure," *Applied Physics Letters*, vol. 56, pp. 770-772, 1990.
- [45] A. Fathimulla, H. Hier, L. Aina, T. Worchesky and P. Uppal, "InP-Based Multi-Wavelength QWIP Technology," *Proceedings of SPIE*, vol. 5406, pp. 589-599, 2004.
- [46] S. Ozer, U. Tumkaya and C. Besikci, "Large Format AlInAs-InGaAs Quantum Well Infrared Photodetector Focal Plane Array for Midwavelength Infrared Thermal Imaging," *IEEE Photonics Technology Letter*, vol. 19, pp. 1371-1373, 2007.
- [47] S. Adachi, "GaAs, AlAs, and $\text{Al}_x\text{Ga}_{1-x}\text{As}$: Material Parameters for Use in Research and Device Applications," *Journal of Applied Physics*, vol. 58, pp. R1-R29, 1985.
- [48] T. Pearsall, *GaInAsP Alloy Semiconductors*, John Wiley and Sons, 1982.
- [49] H. Schneider, M. Walther, C. Schonbein, R. Rehm, J. Fleissner, W. Pletschen, J. Braunstein, P. Koidl, G. Weimann, J. Ziegler and W. Cabanski, "QWIP FPAs for High-Performance Thermal Imaging," *Physica E*, vol. 7, pp. 101-107, 2000.
- [50] S. U. Eker, Y. Arslan and C. Beşikci, "High Speed QWIP FPAs on InP Substrate," *Infrared Physics and Technology*, vol.54, pp. 209-214, 2011.
- [51] Y. Yang, H. Liu, W. Shen, N. Li, W. Lu, Z. Wasilewski and M. Buchanan, "Optimal Doping Density for Quantum Well Infrared Photodetector Performance," *IEEE Journal of Quantum Electronics*, vol. 45, pp. 623-628, 2009.
- [52] M. Kaldırım, "Dual and Single Color Mid-Wavelength Infrared Quantum Well Photodetectors," M.Sc. Thesis, METU, 2008.
- [53] S. Gunapala, B.F. Levine, D. Ritter, R. Hamm and M. Panish, "InGaAs/InP Long Wavelength Quantum Well Infrared Photodetectors," *Applied Physics Letters*, vol. 58, pp. 2024-2026, 1991.

- [54] R. Rehm, H. Schneider, M. Walther, P. Koidl and G. Weimann, "Avalanche Multiplication Due to Impact Ionization in Quantum-Well Infrared Photodetectors: A Quantitative Approach," *Applied Physics Letters*, vol. 82, pp. 2907-2909, 2003.